UNIVERSITY OF CALIFORNIA SAN DIEGO

Indirect Exciton Propagation in van der Waals Heterostructures

A Dissertation submitted in partial satisfaction of the requirements
for the degree of Doctor of Philosophy

in

Materials Science and Engineering

by

Lewis H. Fowler-Gerace

Committee in charge:

Professor Leonid Butov, Chair
Professor Monica Allen, Co-Chair
Professor Shadi Dayeh
Professor Michael Fogler
Professor Brian Maple

2022

The Dissertation of Lewis H. Fowler-Gerace is approved, and it is acceptable in quality and form for publication on microfilm and electronically.

University of California San Diego

2022

EPIGRAPH

See that the imagination of nature is far, far greater than the imagination of man.

– Richard Feynman

TABLE OF CONTENTS

LIST OF FIGURES

ACKNOWLEDGEMENTS

I would like to thank my advisor Professor Leonid Butov for his patience and dedication to training me as a scientist. His rigorous approach to experimental research serves as a guidepost which I will take with me for the rest of my career.

I am thankful for the senior class of graduate students when I joined the lab: Erica Calman for teaching me about optics, Chelsey Dorow for her humor, Matt Hasling for his excellent hats. I would like to thank my coworker Darius Choksy for helping me talk through my experiments when I encountered problems (which was often). I also thank Dr. Ryan Nichols and Dr. Sheng Hu for valuable discussions during a critical stage of my project when I was adapting a fabrication procedure to work within the UCSD cleanroom facilities.

Finally, I would like to thank my friends and family for all their support. My parents provided both an ear for my problems, as well as a helpful nudge to keep moving when the going was rough. My friends have provided me with an incredible level of support, giving me a mental escape from my work whenever I needed it.

The text of chapter 3, in part, is a reprint of the material as it appears in E. V. Calman, L. H. Fowler-Gerace, D. J. Choksy, L. V. Butov, D. E. Nikonov, I. A. Young, S. Hu, A. Mischenko, and A. K. Geim, Indirect Excitons and Trions in $MoSe_2/WSe_2$ van der Waals Heterostructures. *Nano Lett*. 20, 1869 (2020). © American Chemical Society, where the dissertation author is the co-first author. The co-authors in these publications directed, supervised, and co-worked on the research which forms the basis of this chapter.

The text of chapter 4, in part, is a reprint of the material as it appears in L. H. Fowler-Gerace, D. J. Choksy, and L. V. Butov, Voltage-controlled long-range propagation of indirect

excitons in a van der Waals heterostructure. *Phys. Rev. B*, 104, 165302 (2021). © American Physical Society, where the dissertation author is the first author. The co-authors in these publications directed, supervised, and co-worked on the research which forms the basis of this chapter.

The text of chapter 5, in part, has been submitted for publication of the material, L. H. Fowler-Gerace, Z. Zhou, E. A. Szwed, and L. V. Butov, Long-range quantum transport of indirect excitons in van der Waals heterostructure, https://arxiv.org/abs/2204.09760 (2022), where the dissertation author is the first author. The co-authors in these publications directed, supervised, and co-worked on the research which forms the basis of this chapter.

VITA

2015	B. A. in Physics, Wesleyan University
2015	Quality Assurance Intern, TRACON Pharmaceuticals, Inc.
2016	M. S. in Materials Science and Engineering, Department of Mechanical and Aerospace Engineering University of California San Diego
2017	Graduate Teaching Assistant, Department of Chemistry, University of California San Diego
2022	Ph. D. in Materials Science and Engineering, Department of Mechanical and Aerospace Engineering University of California San Diego

PUBLICATIONS

L. H. Fowler-Gerace, Z. Zhou, E. A. Szwed, and L. V. Butov, Long-range quantum transport of indirect excitons in van der Waals heterostructure, https://arxiv.org/abs/2204.09760

L. H. Fowler-Gerace, D. J. Choksy, and L. V. Butov, Voltage-controlled long-range propagation of indirect excitons in a van der Waals heterostructure. *Phys. Rev. B*, 104, 165302 (2021)

E. V. Calman*, L. H. Fowler-Gerace*, D. J. Choksy, L. V. Butov, D. E. Nikonov, I. A. Young, S. Hu, A. Mischenko, and A. K. Geim, Indirect Excitons and Trions in $MoSe_2/WSe_2$ van der Waals Heterostructures. *Nano Lett*. 20, 1869 (2020)
*equal contribution

L. R. Smith, L. Fowler-Gerace, and R. L. Lieber, Muscle extracellular matrix applies a transverse stress on fibers with axial strain, Journal of biomechanics 44, 1618 (2011)

ABSTRACT OF THE DISSERTATION

Indirect Exciton Propagation in van der Waals Heterostructures

by

Lewis H. Fowler-Gerace

Doctor of Philosophy in Materials Science and Engineering

University of California San Diego, 2022

Professor Leonid Butov, Chair
Professor Monica Allen, Co-Chair

Spatially indirect excitons (IXs), also known as interlayer excitons, are bound pairs of an electron and a hole in spatially separated layers. IXs can propagate over long distances before they recombine into light, and they can cool down below the temperature of quantum degeneracy within their lifetimes, which can be controlled by gate voltage up to microseconds and beyond. These properties make IXs a promising platform for studying fundamental physics phenomena and as the medium for highly efficient signal processing devices. IXs were originally studied in gallium arsenide (GaAs) heterostructures, where IXs have shown evidence for Bose-Einstein condensation, and proof of principle has been demonstrated for excitonic transistors and

excitonic integrated circuits. IXs only exist at low temperatures in GaAs systems due to the low IX binding energy on the order of 10 meV. In the transition-metal dichalcogenide (TMD) heterostructure system, the IX binding energy is predicted to be more than two orders of magnitude higher, making IXs stable at room temperature and allowing for the possibility of high temperature IX superfluidity. To date, observation of some of the key IX behaviors, namely the long-range IX transport and evidence of IX condensation, has remained elusive in the TMD system. This dissertation characterizes the IX spectrum in a $MoSe_2/WSe_2$ heterostructure, demonstrates the realization and control of long-range IX propagation using a new mechanism beyond the know mechanism for IX control in GaAs heterostructures, and separately identifies a quantum origin for the propagation of IXs generated by resonant excitation in the TMD heterostructure.

Chapter 1

Introduction to Indirect Excitons

1.1 Background

Over the last half a century, computers have reached near ubiquity in modern life. Their cost has decreased, and computational power has increased by many orders of magnitude over that time. In 1965, Gordon E. Moore speculated that the number of transistors that could fit onto a square of silicon would roughly double every two years [1], and this progress, dubbed Moore's law, has held nearly constant for almost fifty years. However, in the last decade, this trend appears to be slowly down, and the gains in transistor density come at a much greater cost in terms of the state-of-the-art fabrication equipment need to sustain such year-over-year improvements [2]. Many different approaches have been employed to meet the demand for increased computational power, such as advanced lithographic processes, more efficient algorithms, and even fundamentally different computation architectures such as quantum computers. Another exotic computer could be based on a new computation state variable- the excitonic state, different from the electronic state used in conventional computers. Although the field of excitonic computation is still in its infancy, there has been substantial interest in studying these systems, because they offer the possibility of highly efficient signal processing, direct conversion with light for computation involving optical inputs and outputs, and nanoscale size limited only by the exciton de Broglie wavelength and Bohr radius, which can reach on the order of nanometers [3].

1.2 Excitonic Computation

In an electronic transistor, information is carried by the electric potential of the device relative to some threshold. Below that threshold, the device is off, at logic 0, and above that threshold the device is on, at logic 1—chaining many transistors together allows encoding arbitrary strings of 1s and 0s, forming the basis for modern computational electronics. An excitonic transistor can operate on a similar principle, except the relevant threshold is relative to the excitonic potential, different from the electronic potential [4,5]. To perform computations, many transistors need to change states from off to on and vice versa. Switching between states involves moving charges across the threshold potential difference (e.g. the gate potential in a metal-oxide field effect transistor), which is approximately one volt in silicon based electronics. Since conventional transistor have finite resistances, charging up the transistor across 1 volt consumes energy, and that energy is dissipated as heat in the system. Heat dissipation is one of the limitations in designing systems with greater transistor density—this contributes to why the CPU on a computer extends primarily in two dimensions—the third dimension cannot be equally utilized, or the chip would overheat. In contrast, the ideal excitonic transistor could operate around a much lower threshold difference between its off and on state, and this lower switching voltage could dramatically reduce the energy required and heat dissipated [3].

1.3 Direct and Indirect Excitons

Excitons offer the possibility for high efficiency devices due to their fundamental nature as bosonic particles. Unlike fermionic electrons, excitons are composite particles consisting of both an electron and a hole, bound together by the coulomb force. Direct excitons (DXs) consist of an electron and hole confined in the same spatial layer of a material. For optically generated

DXs, the positively charged vacancy, or hole, produced by an electron leaving the valence band interacts with the negatively charged electron in the conduction band via the coulomb force. This interaction lowers the energy of the composite particle, making it the energetically favorable state with the energy $E_{\mathrm{DX}} = E_{\mathrm{g}} - E_{\mathrm{Ry,DX}}$ where E_{g} is the band gap of the material and $E_{\mathrm{Ry,DX}}$ is the binding energy of the direct exciton within the Bohr model. When the electron and the hole exist within the valence and conduction bands of the same layer of the material (Figure 1.1b), the lifetime of the particle before it recombines into light is very short, on the order of tens of picoseconds [6]. In order for excitons to travel over meaningful distances, e.g. the dimensions of an excitonic device, the lifetime of the particle needs to be extended to much longer timescales. This is accomplished by separating the electron and the hole that comprise the exciton into physically different layers of a material, for example into two coupled quantum wells of a gallium arsenide (GaAs) heterostructure (Figure 1.1a,b) [7].

The exciton with electron and hole in spatially separated layers is called a spatially indirect exciton, or interlayer exciton (IX). Their spatial separation gives IXs a permanent out-of-plane dipole, which allows for controlling the IX energy (figure 1.1b,c) and lifetime by an applied electric field, where $E_{\mathrm{IX}} = E_{\mathrm{g}} - E_{\mathrm{Ry,IX}} - ed_{\mathrm{z}}F_{\mathrm{z}}$ (e the electron charge, d_{z} the separation distance between quantum well layers, F_{z} the applied electric field), and the reduction in IX

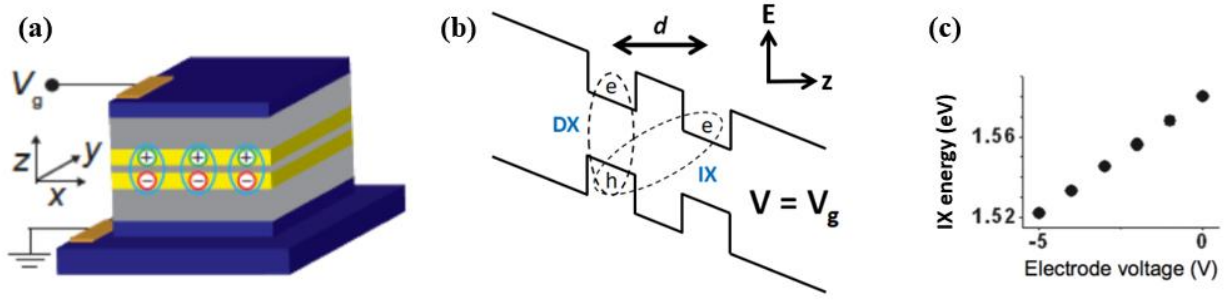

Figure 1.1: Schematic for IX formation. (a) Schematic real-space layer diagram of a coupled quantum well GaAs heterostructure. (b) Schematic energy band diagram showing DXs and IXs. (c) IX energy change with applied voltage.

energy with applied field is accompanied by an increase in the IX lifetime by orders of magnitude [8]. The long lifetimes allow IXs to cool down to the lattice temperature of the material in which they exist, and in turn, cool down below the temperature of quantum degeneracy $T_{\mathrm{d}} = 2\pi\hbar^2 n/k_{\mathrm{B}} m$ (n the exciton density, m the exciton mass) and form a condensate in momentum space [9]. Evidence for IX condensation in GaAs heterostructures has been observed in terms of: huge broadband noise in the IX luminescence and lifetimes [10]; large increase in the exciton diffusivity and radiative decay rate [11]; stimulated scattering into low energy states [12]; macroscopic long-range order in the exciton state [13]; enhancement of the coherence length well beyond the classical value [14]; and long scattering times for ballistic IX propagation [15]. Such condensates can exhibit vanishing resistance to propagation and strongly suppressed thermal tails in the IX energy distribution, offering the opportunity to develop highly energy efficient excitonic devices [3].

Along with their long lifetimes, the second property of IXs that facilitates their propagation over long distances is the repulsive IX interaction originating from their permanent out-of-plane dipole moment. Even the highest quality quantum well systems contain defects or alloy fluctuations in the layer interfaces, and these factors introduce random potentials in the in-plane energy landscape felt by IXs which can lead to IX localization [16]. The repulsive IX interaction [17] means that sufficient IX density can screen these random potentials, like water filling in the bumps and cracks in pavement. The screened in-plane potentials provide a smaller barrier to the exciton propagation [18], and IX propagation over hundreds of microns has been observed in the GaAs heterostructure system [19].

Control of IX propagation is achieved by applied electric field across the heterostructure which shapes the in-plane variation of the exciton potential. IXs follow the energy gradient, so a

variation in the voltage applied to the electrodes can create a controllable energy landscape that produces a directional drift current of indirect excitons [20]. Variations on this method have been exploited to realize numerous devices for directing exciton propagation, such as ramps [21], conveyers [22], and traps [23]. The kinetics of IX propagation within these and many other potential landscapes is well described by the drift-diffusion model for IXs developed in [24] (see also section 5.3 in this thesis).

The long-range IX propagation, facilitated by long lifetimes and disorder screening, along with the control of IX drift current by applied voltage, enabled the realization of proof-of-principle excitonic transistors [5] and integrated circuits [25]. In these devices, the IX transistor was switched from off to on by a gate electrode which controlled a barrier to IX transport. The voltage on the gate was switched around a threshold which controlled whether the IXs can propagate across the barrier, and the width of the IX energy distribution contributes to the efficiency of the device. The highest efficiency would be realized when the IX system is condensed into a single state below the temperature of quantum degeneracy. However, realistic exitonic devices should be robust at easily achievable temperatures to minimize the energy cost of the entire system. The limitation of IXs is that they can only exist at temperatures roughly below $E_{\mathrm{Ry,IX}}/k_{\mathrm{B}}$ [26]. In the GaAs/AlGaAs systems, $E_{\mathrm{Ry,IX}}$ is around 4 meV [27], reaching 10meV in GaAs/AlAs type II heterostructures [28], and up to 30meV in ZnO heterostructures [29]. These low binding energies make IXs in these heterostructures stable only at low temperatures, and the coherence phenomena discussed above only observed in GaAs below approximately a few degrees Kelvin [14]. In the low temperature regime, devices based on indirect excitons would be impractical for anything beyond research or space-based applications, where low temperatures are only accessible at great expense.

1.4 Indirect Excitons in Transition-Metal Dichalcogenides

In the last decade, a class of 2-dimensional materials called transition-metal dichalcogenides (TMDs) has emerged with possible applications from wearable electronics to solar cells to transistor electronics, boasting impressive flexibility, transparency, and charge carrier mobility [30,31]. The TMD materials are two-dimensional sheets comprised of a transition-metal such as tungsten or molybdenum, sandwiched in between two layers of chalcogen atoms like sulfur or selenium. Materials within this class can be grown as crystals of macroscopic dimension with the layers of held together by the van der Waals force, or synthesized as a single layer in a laboratory using a technique such as chemical vapor deposition. Isolated single layers of these materials have an atomic thickness of less than one nanometer [32] and show changes in their optical and electronic response as a function of the number of layers. When the thickness of these materials is reduced from bulk thickness to a single monolayer, they transition from an indirect band gap to a direct band gap semiconductor, resulting in their strong light-matter interaction and efficient photoluminescence [33,34]. This strong optical response makes them a promising platform for the development of excitonic devices.

The IX binding energy within a quantum well system depends on the strength of the coulomb interaction, and the coulomb interaction scales as $1/\varepsilon d_z$ (d_z is the separation distance between the quantum well layers, ε the dielectric constant of the material). In the TMD system, the quantum well layers are two monolayer TMDs stacked together. Both the reduced distance between the electron and hole layers (~ 1nm for TMD vs. ~ 10nm for GaAs), and the lower out-of-plane dielectric constant (~ 7 for TMDs vs. ~ 12 for GaAs) [35,36] contributes to the much larger IX binding energy, predicted to be up to 350meV for TMD heterostructure systems [37]. This high binding energy makes IXs robust at room temperature and raises the maximum IX

density that can be achieved before dissociation at the Mott transition into an electron-hole plasma, which in turn leads to a predicted high temperature of quantum degeneracy for IXs [38].

1.5 Crystal Structure of TMD Materials

Observation of IXs in the TMD system is complicated by the crystal structure of the monolayer materials. The materials are direct gap semiconductors with a hexagonal crystal lattice and a conduction and valence band minima at the K and K' valleys in the Brillouin zone, with the two valleys connected by time-reversal symmetry [39]. IXs within a TMD heterostructure exist with the electron layer occupying the conduction band of one monolayer and the hole layer within the valence band of the other monolayer. The relative orientation of the crystal axes of the two monolayers can lead to a finite center-of-mass momentum mismatch between the electrons and holes at the K-points within the respective monolayers, and if the mismatch is large enough, the ground state IX will exist with a momentum well outside the light cone [40]. The momentum mismatch between electron and hole leads to greatly suppressed optical response unless the crystal axes of the monolayers are aligned within 0 (AA stacking, R-type) or 60 (AB stacking, H-type) degrees of each other [41].

Mechanically stacking together monolayer crystals inevitably results in some degree of crystal lattice angle mismatch between the two layers. An angle mismatch between the crystal lattice axes of the materials, along with any mismatch in the lattice constants of the materials, causes the formation of a moiré superlattice. The moiré superlattice results from the periodic variation in the positions of the atoms of each layer relative to one another within the plane of the heterostructure, and in turn produces a locally varying bandgap with the period $b = a/\sqrt{\delta\phi^2 + \delta\theta^2}$, where a is the lattice constant, $\delta\phi$ is the lattice constant mismatch, $\delta\theta$ is the

twist angle deviation from either 0 or 60 degree crystal axis alignment between the layers. The moiré pattern has been directly imaged by scanning tunneling microscopy for lattice mismatched [42] and twisted [43] TMD bilayers. The moiré superlattice potential is predicted to cause modulations in the IX energy of ~ 25 and 100 meV, for AB and AA stacking, respectively [44,45]. For very small twist angles (close to 0 or 60 degrees) the lattice angle misalignment can lead to discreet reconstructed domains of perfect crystallographic alignment separated by domain walls, where the degree of atomic reconstruction depends on the decrease in stacking energy from adopting reconstructed domains relative to the increased intralayer strain energy [46].

1.6 IX Localization and Propagation within the TMD System

Studies of IXs in TMD systems began with identifying the key features of IX luminescence, namely the energy shift with voltage, the IX repulsive interaction, the long IX lifetime, and the observation and control of IXs at room temperature [47–49]. However, despite long IX lifetimes, observation of long-range propagation of IXs, one of the key requirements for development of excitonic devices, has remained elusive. Relatively short-range IX propagation over a few microns has been reported [50–58], but the absence of propagation lengths on the same order of magnitude as observed in GaAs systems can be related to the presence of the moiré superlattice potentials. TMD heterostructures synthesized by chemical vapor deposition *in situ* can exhibit perfect alignment between the crystal axes of the two layers [59] (using monolayers with the same chalcogen atoms leads to a low lattice constant mismatch < 0.3% [60]). However, current monolayer deposition techniques produce TMD monolayers with reduced quality, as evidence by the larger linewidth of the direct exciton luminescence [61]. The

larger linewidth implies a greater disorder potential felt by IXs in the material, and this disorder potential may also play a substantial role in localizing IXs and suppressing their transport.

Along with the disorder potentials, variations in the exciton potential caused by moiré superlattices is predicted to be an obstacle to exciton transport, and observations of IX transport in the presence of these potentials is a key milestone for the development of IX devices in the TMD heterostructure system.

1.7 Outline of the Dissertation

Following the introductory chapter, chapter 2 of this thesis presents the methods for TMD sample fabrication and the optical spectroscopy employed as the main experimental technique. Chapters 3, 4, and 5 form body of this thesis, presenting: (i) identification of the characteristic spectral features of the IX luminescence within the $MoSe_2/WSe_2$ TMD heterostructure system; (ii) the observation of voltage-controlled IX propagation in the presence of the predicted localization potentials; (iii) resonant-enhanced long-range IX propagation that goes beyond the known mechanisms for IX propagation within the classical drift-diffusion model, suggesting a quantum origin to the propagation. The texts in each of chapters 3, 4, and 5 are presented as stand-alone works and follow from the published or submitted manuscripts.

Chapter 2

Experimental Methods

2.1 Sample Fabrication

The work reported in chapter 3 was performed in part on a sample fabricated in the University of Manchester, UK, in the lab of Andre Geim, and in part on a sample fabricated at the cleanroom at UCSD. The cleanroom provides a dust-free environment with a controlled and low humidity. The work in chapter 4 and 5 was performed entirely on the sample fabricated at UCSD.

The van der Waals heterostructure was assembled using the dry-transfer peel-and-lift technique [62]. Crystals of hBN, $MoSe_2$, and WSe_2 were first mechanically exfoliated onto Si/SiO_2 substrates that were coated with a double polymer layer consisting of polymethyl glutarimide (PMGI) and polymethyl methacrylate (PMMA). The 300nm SiO2 top layer of the substrate wafer helped to distinguish between monolayer or thicker regions using optical contrast [63]. The bottom PMGI was then dissolved with the tetramethylammonium hydroxide based solvent CD-26, causing the top PMMA membrane with the target 2D crystal to float on top of the solvent. The PMMA membrane functioned both as a support substrate for transferring the crystal and as a barrier to protect the crystal from the solvent. Separately, a large graphite crystal was exfoliated onto an oxidized Si wafer, which served as the basis for the heterostructure. The PMMA membrane supporting the target crystal was then flipped over and aligned above a flat region of the graphite crystal using a micromechanical transfer stage (figure 2.1). The two crystals were brought into contact and the temperature of the stage was ramped to

80° C in order to increase adhesion between the 2D crystals and weaken the adhesion between the PMMA membrane and the crystal. Then, the PMMA membrane was peeled off leaving the bilayer stack on the wafer. The procedure was repeated leading to a multi-crystal stack with the desired layer sequence.

The long WSe_2 and $MoSe_2$ edges reach ~ 30 and ~ 20 μm, respectively, which enables a rotational alignment between the WSe_2 and $MoSe_2$ monolayers. The twist angle estimated from the angle between the long WSe_2 and $MoSe_2$ edges $\delta\theta = 0.5° \pm 0.8°$ (Figure 3.6)

Substantial efforts were made in the initial adaptation of the procedure to select the ideal tape for the mechanical exfoliation. The selected tape is the G-65 variant produced by Adwill, used industrially in the silicon wafer dicing process. The tape should be extremely low residue to reduce the possibility of contamination and have an intermediate stiffness that does not crack the TMD materials during the exfoliation process. The adhesive strength of the tape should be greater than the van der Waals attraction between the layers of the TMD bulk material, but not so much that it damages the polymer membrane regions outside the TMD crystal area.

Selection of the photoresist thickness that functions at the polymer membrane is also important. Optimal thicknesses of the resist were determined to be ~ 300 nm for the PMMA top layer and ~ 700 nm for the PMGI undercut layer. The optical contrast method used to identify the monolayer regions of the TMD materials favors thinner polymer layers. However, if the polymer layers are too thin, the dry transfer procedure has a large chance of failing due to tearing of the membrane. The ~ 1 μm total thickness allows for identification of monolayer regions while preserving a robust transfer process with a high chance of success.

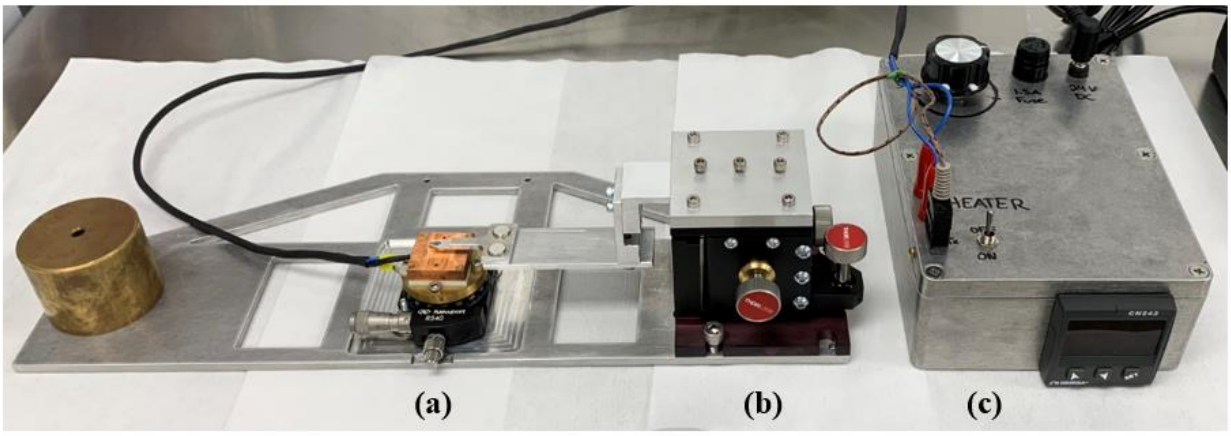

Figure 2.1: Micromechanical transfer stage. (a) Heater block on top of the rotational alignment stage. (b) Flexure translation stage. (c) PID loop heater control box with programmable set temperature and adjustable heater power.

The micromechanical transfer stage consisted of a frame that supported a rotational alignment stage with an accuracy of ~ 0.5 degrees, a homebuilt heater stage with PID loop temperature control, and a flexure translation stage for aligning the crystal supported by the polymer membrane above the substrate silicon wafer attached to the heater stage. The flexure stage has ultra-high linearity, so translation in one axis is completely decoupled from the other two axes, critical for the precise alignment of the monolayers.

Electrical contacts to the heterostructure were patterned using standard optical lithography, and liftoff was performed alongside annealing in Remover PG, an N-methyl-2-pyrrolidone (NMP) based solvent stripper, at 70° C for 12 hours. No ultrasonication was used during the lift off step, because the ultrasonication can cause the TMD layers to lift up into the solution.

2.2 Optical Measurements

Optical experiments were taken using a HeNe laser, a TiSaph laser with tunable

excitation energy in continuous wave (cw) mode, or a pulsed diode laser for time-resolved kinetics measurements. Luminescence spectra were measured using a spectrometer with resolution 0.2 meV and a liquid-nitrogen-cooled charge-coupled detector (CCD). The experiments were performed in a variable-temperature 4He cryostat, primarily operating at 1.7 K. For the kinetics measurements, a PicoStar HR TauTec time-gated intensifier was inserted in between the spectrometer and the CCD.

TMD heterostructures with samples areas of around 10-20 μm x 10-20 μm show substantial heterogeneity both in the intensity and the energy of the IX luminescence over length scales comparable to the optical resolution of the setup of around 1 μm. Sample drift inside the cryostat was observed on the order of 5-10 μm per hour, which was almost unnoticeable in the larger, more homogeneous GaAs heterostructures but quite problematic in the TMD system—limiting the positioning accuracy of the laser spot on the sample and the maximum exposure time before the sample drifted out of focus. The sample drift comes from fluctuations in the position of the sample inside the cryostat, relative to the position of the focusing objective outside the cryostat. The results presented in chapter 3 and 4 primarily used this setup with the objective outside the cryostat.

The experimental accuracy was later improved substantially by replacing the objective outside the cryostat with a smaller aspheric focusing lens inside the cryostat, with an Attocube xyz piezo translation stage allowing for precise sample positioning and focusing. Since the objective was inside the cryostat at the same temperature as the sample, fluctuations simultaneously affected both the sample and the focusing lens, resulting in greatly reduced sample drift relative to the focusing lens of less than 1 μm over 4 hours. The numerical aperture of the focusing lens was improved to 0.64, which resulted in a nearly diffraction limited spot size

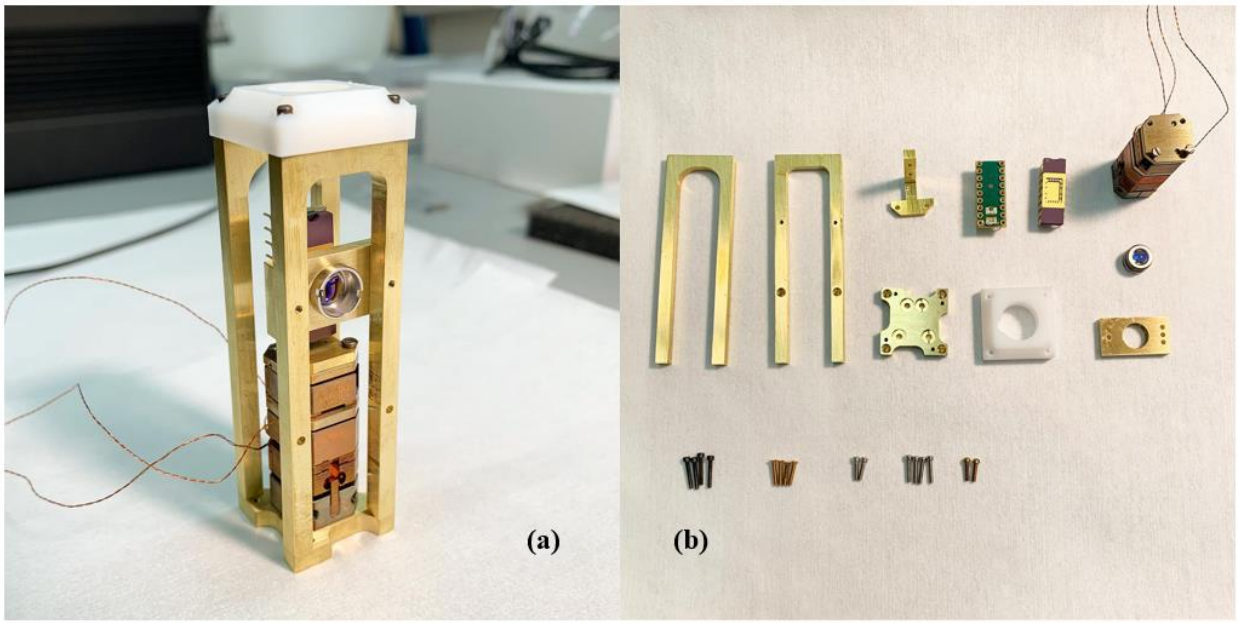

Figure 2.2: Sample positioner stage. (a) Assembled focusing lens mount and sample positioner. (b) Individual components. The Attocube xyz positioner is at the top right. The aspheric focusing lens is just below the positioner

of ~1.5 μm with a spatial resolution of better than 1 μm. The small space inside the cryostat necessitated a home-built lens, sample, and piezo stage mount (fig. 2.2). One of the consequences of using an aspheric lens instead of an achromatic objective was the change in the focus of the emitted light as a function of the wavelength. Since the laser excitation and the IX luminescence are separated in wavelength by more than 200 nm, an additional focusing telescope was placed in the detection path of the experimental setup, which allowed for tuning the focus of the emission to the desired wavelength while preserving a diffraction-limited laser excitation spot.

The improved sample stability made it possible to perform the IX kinetics measurements, where the exposure time must be made much longer to compensate for the greatly reduced signal. A cost-effective method for tuning a diode laser energy is by simply heating up the diode. The semiconductor effective band gap reduces with increasing temperature, resulting in the laser energy lowering by around 0.2 nm per degree Celsius of temperature increase, mostly linear

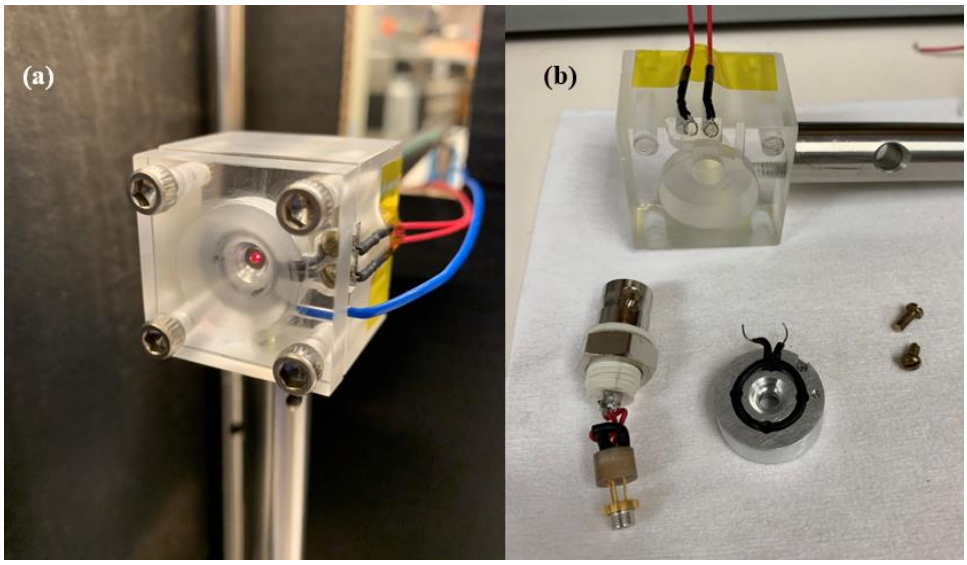

Figure 2.3: Laser diode heater. (a) Assembled semiconductor laser diode mount and heater. (b) Individual parts. Top: PMMA block housing the heater chuck and BNC socket. Bottom left: laser diode mounted to a BNC cable connector. Bottom right: Heater chuck machined for good thermal contact with the diode can enclosure, and with insulated nichrome heater wire running through the grooves in the metal. The two leads were connected to an adjustable DC power supply and the temperature was monitored by a thermocouple attached to the heater chuck [blue wire in (a)].

within the operating range of the laser from 0° to 50° C. The pulsed laser diode used in the work in chapter 5 was heated to 50° C, which red-shifted the laser wavelength by approximately 6nm to tune it to the one of the DX resonances in the sample. The heating was accomplished using a home-built diode heater connected to a DC power supply. The heater was constructed to minimize the thermal flux required to keep the diode warm, which minimized excessive thermal gradients that cause the laser diode spot to drift over time.

Chapter 3

Neutral and Charged Indirect Excitons

3.1 Introduction

An indirect exciton (IX), also known as an interlayer exciton, is a bound pair of an electron and a hole confined in spatially separated layers. The spatial separation between the electron and hole layers allows achieving long IX lifetimes, orders of magnitude longer than lifetimes of direct excitons (DXs) [9]. Due to their long lifetimes, IXs can cool below the temperature of quantum degeneracy [12]. The realization of IX quantum Bose gases in GaAs heterostructures led to finding of many phenomena, including spontaneous coherence and condensation of IXs [14], the spatially modulated exciton state [13,64], the commensurability effect of exciton density waves [65], spin textures [66], and the Pancharatnam-Berry phase and long-range coherent spin transport in the IX condensate [67].

Furthermore, an IX has a built-in electric dipole moment, ed_z (d_z is the separation between the electron and hole layers). As a result, IX energy, lifetime, and flux can be effectively controlled by voltage that is explored for the development of excitonic devices. In GaAs heterostructures, experimental proof-of-principle demonstrations were performed for excitonic ramps [20,68], excitonic acoustic-wave [69] and electrostatic [22] conveyers, and excitonic transistors [25].

However, the IX range of existence in GaAs heterostructures is limited to low temperatures due to low IX binding energies. Excitons exist in the temperature range roughly

below $E_{\mathrm{Ry,IX}}/k_{\mathrm{B}}$ ($E_{\mathrm{Ry,IX}}$ is the exciton binding energy, k_{B} is the Boltzmann constant) [26]. The IX binding energy in GaAs/AlGaAs heterostructures is typically ~ 4 meV [27]. The maximum $E_{\mathrm{Ry,IX}}$ in GaAs heterostructures is achieved in GaAs/AlAs coupled quantum wells (CQW) and is ~ 10 meV [28]. The temperature of quantum degeneracy, which can be achieved with increasing density before excitons dissociation to electron-hole plasma, also scales proportionally to $E_{\mathrm{Ry,IX}}$ [38]. In GaAs heterostructures, quantum degeneracy was achieved below few Kelvin [12] and the proof of principle for the operation of IX switching devices was demonstrated below ~ 100 K [70]. IXs with high $E_{\mathrm{Ry,IX}}$ reaching ~ 30 meV are explored in ZnO and GaN heterostructures [29,71–73].

Van der Waals heterostructures composed of atomically thin layers of TMD offer an opportunity to realize artificial materials with designable properties [31] and, in particular, allow the realization of excitons with remarkably high binding energies [74,75]. IXs in TMD heterostructures are characterized by binding energies exceeding 100 meV making them stable at room temperature [38]. IXs were observed at room temperature in TMD heterostructures [49]. Due to the high IX binding energy, TMD heterostructures can form a material platform both for exploring high-temperature quantum Bose gases of IXs and for creating realistic excitonic devices.

IXs are intensively studied in optically excited van der Waals TMD heterostructures with coupled electron and hole layers [40,44,45,47–49,51,52,76–94]. IXs can also appear in electron-electron (or hole-hole) bilayers in a collective electronic state in strong magnetic fields at the total Landau level filling factor 1. The latter was realized in GaAs heterostructures [95–100] and in graphene—boron-nitride—graphene van der Waals heterostructures [101,102].

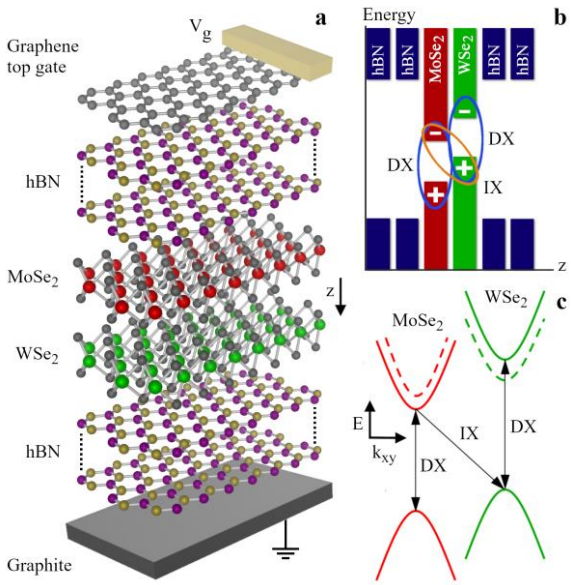

Figure 3.1: Van der Waals $MoSe_2/WSe_2$ heterostructure. The heterostructure layer (a) and real space energy band (b) diagrams. The ovals indicate a direct exciton (DX) and an indirect exciton (IX) composed of an electron (−) and a hole (+). (c) Momentum space energy band diagram around the K point. Solid and dashed lines represent spin-up and spin-down bands. Optically active low-energy DX and IX states are indicated by arrows.

3.2 Results and Discussion

In this work, we present studies of IXs in $MoSe_2/WSe_2$ heterostructures. We report on the observation of charged IXs, i.e. indirect trions (IX^T). The identification of indirect trions is based on the measured energy splitting and temperature dependence of IX and IX^T luminescence lines: The splitting corresponds to the binding energy for negative indirect trions in TMD heterostructures calculated in Ref. [37] and the temperature dependence follows the mass action law for the indirect trions. We also report on the realization of IXs with a luminescence linewidth reaching 4 meV at low temperatures, the lowest value reported so far for IXs in TMD heterostructures. An enhancement of IX luminescence intensity and the narrow linewidth are observed in localized spots.

The $MoSe_2/WSe_2$ heterostructures were assembled by stacking mechanically exfoliated

2D crystals on a graphite substrate (Figure 3.1a). The CQW is formed where the $MoSe_2$ and WSe_2 monolayers overlap. The $MoSe_2$ and WSe_2 monolayers are encapsulated by hexagonal boron nitride (hBN) serving as dielectric cladding layers. The real-space energy-band diagram is shown in Figure 3.1b. IXs are formed from electrons and holes confined in adjacent monolayer $MoSe_2$ and WSe_2, respectively. These type-II $MoSe_2/WSe_2$ heterostructures with staggered band alignment are similar to AlAs/GaAs CQW where IXs are formed from electrons and holes confined in adjacent AlAs and GaAs layers, respectively [28,70]. In the $MoSe_2/WSe_2$ heterostructures, due to the order of spin-up and spin-down states in valence and conduction bands (VB and CB) the lowest energy DX state is optically active in $MoSe_2$ and dark in WSe_2, and the lowest energy IX state is optically active (Figure 3.1c) [44,94,103–107]. We studied heterostructures manufactured in Manchester and San Diego (samples M and S). The order of $MoSe_2$ and WSe_2 layers is different in samples M and S to probe both configurations. Both samples show indirect trions and intensity enhancement in localized spots.

Along most of the CQW heterostructure area, the IX luminescence intensity varies only slightly (Figure 3.2a). We will refer to this CQW heterostructure area as the CQW flake. However, we observed bright spots, which exhibit enhanced IX luminescence in comparison to the surrounding regions of the CQW heterostructure (Figure 3.2a, 3.6 and 3.7). The CQW flakes and CQW bright spots show similar features of neutral and charged IX luminenscence and the data for both these regions are presented in this work.

In this paragraph, we outline phenomenological properties of the bright spots. We note that further details of their properties and their origin form the subject for future studies and do not affect the conclusions on neutral and charged IXs in this work. The enhancement of IX luminescence at the bright spots is localized within ~ 2 μm in sample S and within the length

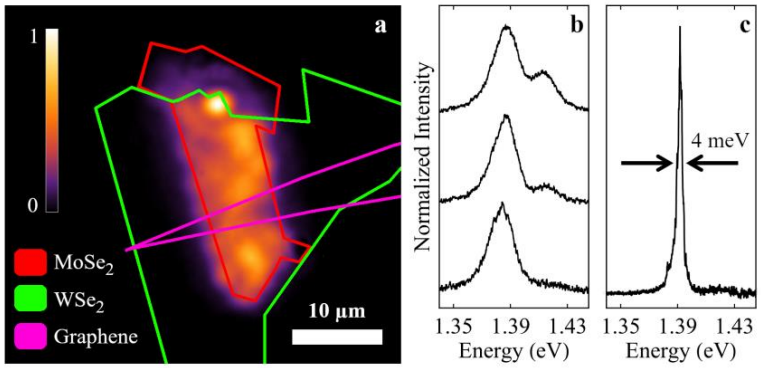

Figure 3.2: IX Luminescence in the CQW flake and bright spot. (a) $\boldsymbol{x}$-$\boldsymbol{y}$ map of indirect luminescence (spectral range 1.24–1.46 eV) in sample S. Indirect luminescence intensity is enhanced in a bright spot observed near the top of the CQW flake. The layer boundaries are shown. (b) The luminescence spectrum at the CQW flake in sample S at excitation power $\boldsymbol{P_{ex}}$ = 3.4, 1, and 0.5 mW (top to bottom). (c) The luminescence spectrum at the bright spot in sample M at $\boldsymbol{P_{ex}}$ = 10 μW. The laser excitation is defocused in (a) and focused at the flake center in sample S (b) and at the bright spot in sample M (c). T = 1.7 K, $\boldsymbol{V_g}$ = 0. All luminescence intensities are normalized.

smaller than the 1 μm optics resolution in sample M. In contrast to IX luminescence, the intralayer DX luminescence varies only slightly along the CQW heterostructure and does not show an intensity enhancement in the bright spots (Figures 3.6 and 3.7). The bright spots form naturally with no artificially designed IX confinement such as in electrostatic traps in GaAs heterostructures [17,108–113]. The presence of the luminescence bright spot for IXs with a built-in electric dipole and its absence for DXs with no electric dipole suggests that the bright spots originate from an accidental IX trapping due to the background electrostatic potential in the heterostructures. The bright spot shows a narrow IX linewidth reaching 4 meV at the lowest excitation power tested (Figures 3.2c and 3.8). The IX linewidth in the bright spot is smaller than the IX linewidths in the rest of the sample.

Two lines of spatially indirect luminescence are observed in the spectrum (Figures 3.2b, 3.3). Due to the IX electric dipole moment, ed_z, the IX energy shifts in the voltage-induced electric field in the z direction, F_z, by $\delta E = -ed_zF_z$. The energy of two luminescence lines is controlled by voltage V_g applied between the graphene top gate and graphite back gate and

creating the bias across the CQW structure (Figure 3.3), indicating that both these lines correspond to spatially indirect luminescence.

The IX line splitting of 28 meV (sample S, Figure 3.2b) [26 meV (sample M, Figure 3.3)] is much smaller than the WSe_2 VB spin-orbit splitting [114]. Therefore, both IX transitions involve holes in the upper VB subband (B excitons considered in Ref. [114] are not involved).

The measured energy splitting and temperature dependence of these two lines identify them as neutral and charged indirect excitons. The lower energy line corresponds to charged IXs, i.e., indirect trions (IX^T), and the higher energy line to neutral IXs (Figure 3.3 right inset).

The energy of the trion luminescence is determined by the difference between the initial state, trion, and final state, remaining electron (for negative trions). At low densities, the IX and IX^T luminescence energies should experience the same shift with voltage following the gap between the VB of WSe_2 and the CB of $MoSe_2$ [37], consistent with the experiment (Figure 3.3). The splitting between the lines corresponds to the trion binding energy. The experimentally found binding energy of the indirect trions of 26–28 meV is in agreement with the calculated binding energy of 28 meV for negative indirect trions in MoS_2/WS_2 heterostructures [37].

Similarly, spatially direct neutral and charged excitons, DX and DX^T, are observed for spatially direct, i.e., intralayer, luminescence (Figure 3.4c). However, in contrast to IX and IX^T, the peak energy of DX and DX^T practically does not change with voltage due to vanishing built-in dipole moment in the direction of applied electric field for direct excitons and trions (Figure 3.3 left inset).

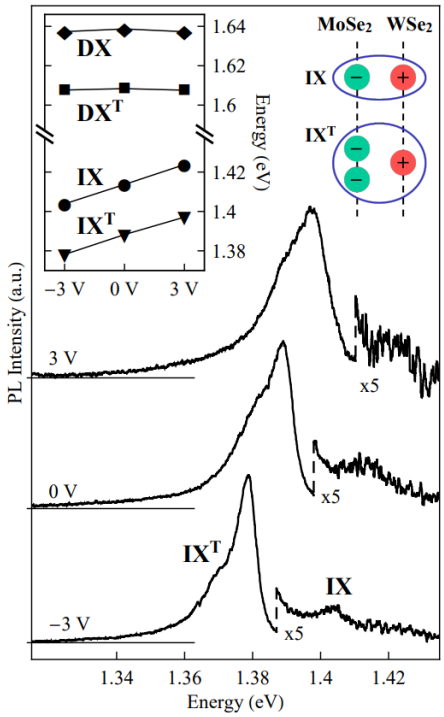

Figure 3.3: Gate voltage dependence of the bright spot. Indirect luminescence spectra in $MoSe_2/WSe_2$ CQW at different gate voltages $\boldsymbol{V_g}$ at the bright spot in sample M. Left inset: Luminescence peak energy vs. $\boldsymbol{V_g}$. IX and IX^T are indirect exciton and trion, DX and DX^T are direct exciton and trion. Right inset: Schematic of IX and IX^T. $\boldsymbol{P_{ex}}$ = 1.25 mW, T = 1.7 K.

The measured indirect trion binding energy of 26–28 meV is smaller than the direct trion binding energy of 32 meV (Figure 3.4) due to the separation between the electron and hole layers, consistent with the theory of indirect trions in GaAs and TMD heterostructures [37,115,116]. DX and DX^T luminescence was studied earlier in monolayer $MoSe_2$ [106,107,117–120].

Further significant support for the asignment of the two lines of spatially indirect luminescence to neutral and charged indirect excitons comes from the temperature dependence: The luminescence intensity ratio of the lines IX^T/IX decreases with increasing temperature (Figure 3.4a,b, Figure 3.5a red symbols, and Figure3.5b symbols) in agreement with the mass action law for the indirect trions (Figure 3.5a red line and Figure 3.5b lines). The relative intensity of the IX^T luminescence decreases with temperature due to the thermal dissociation of

trions. The IX^T temperature dependence is similar to that for DX^T both in earlier studies of DX^T in $MoSe_2$ monolayers [118] and in this work (Figures 3.4 and 3.5).

Solid lines in Figure 3.5 present the simulated ratios of trion and exciton integrated luminescence intensities for the direct, DX^T/DX, and the indirect, IX^T/IX, cases. We simulated these ratios using their approximate proportionality to the densities of corresponding particles. The dependence of the densities on temperature is obtained from the mass action model [118]. In these simulations, the trion binding energy is taken from the measured line splitting. The simulations include two fitting parameters: the densities of background charge carriers n_B and photoexcited electron-hole pairs n_P, their estimation is described in section 3.6. The simulations give qualitatively similar results for various n_P and n_B. At high temperatures, the ratio of trion and exciton densities n_T/n_X increases with reducing temperature, however, at low temperatures, n_T/n_X saturates (Figures 3.5 and 3.11). This saturation is the key characteristic of trion luminescence. The origin of this saturation is in the finite number of background electrons that are involved in the trions. For the trions formed by binding of the background electrons with photoexcited excitons, at low temperatures, the trion density saturates at n_B and, in turn, the ratio n_T/n_X asymptotically approaches $n_B/(n_P - n_B)$. The simulations are in agreement with the experimental data both for direct and indirect trions in the entire temperature range (Figure 3.5).

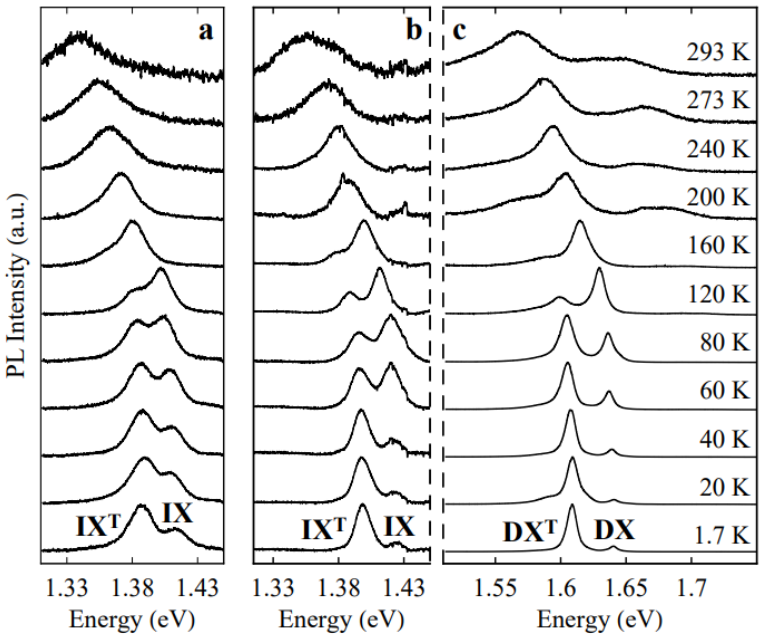

Figure 3.4: Exciton and trion temperature spectra. Spectra of spatially indirect (a,b) and direct (c) luminescence in $MoSe_2/WSe_2$ CQW at different temperatures at CQW flake in sample S (a) and bright spot in sample M (b,c). $\boldsymbol{P_{ex}}$ = 3.4 (a) and 1.25 (b,c) mW, $\boldsymbol{V_g}$ = 0.

As in the type-I MoS_2/hBN TMD heterostructure [49], IXs are observed at room temperature in our type-II heterostructures (Figure 3.4). The observed red shift of the lines with increasing temperature (Figure 3.4) originates from the band gap reduction, which is typical for semiconductors, the TMDs included [118].

The narrowest indirect luminescence linewidth is observed at the lowest temperature (Figure 3.4) and smallest excitation power P_{ex} (Figure 3.8). The indirect luminescence broadens up to ~ 40 meV at room temperature (Figure 3.4). With increasing P_{ex}, the indirect luminescence broadens and shifts to higher energies (Figures 3.2, 3.8). Similar line broadening and shift to higher energies were observed for IXs in GaAs heterostructures and described in terms of repulsive IX interaction [17], which originates from the repulsion of oriented electric dipoles [121–123]. Increasing the density with P_{ex} leads to the enhancement of interaction in the system of indirect excitons and trions and, in turn, the enhancement of IX^T and IX energies.

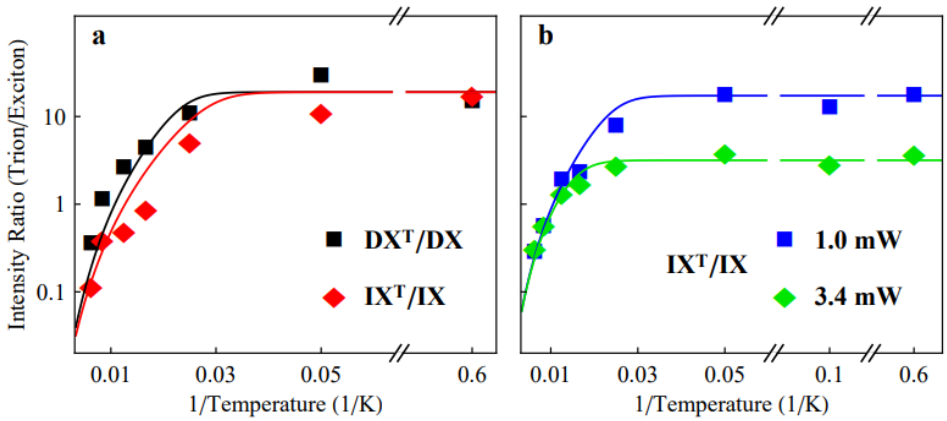

Figure 3.5: Trion/exciton intensity ratio. Experimental (symbols) and simulated (lines) spectrally integrated luminescence intensity ratio IX^T/IX (green, blue, red) and DX^T/DX vs. 1/temperature at the CQW bright spot in sample M (a) and the CQW flake in sample S (b). $\boldsymbol{P_{ex}}$ = 1.25 mW (a), 1 mW [blue squares in (b)], and 3.4 mW [green diamonds in (b)], $\boldsymbol{V_g}$ = 0.

Isolated IX^T have substantial binding energy at low separation between electron and hole layers [37,115,116], relevant for the $MoSe_2/WSe_2$ heterostructure. However, the IX^T binding energy is smaller than the IX binding energy that stabilizes the neutral system of IXs against IX transformations to trions and charged particles. This suggests that most of IX^T form by binding of electrons and holes created by excitation to background charge carriers which are present in the heterostructure due to unintentional doping and CQW layer charging induced by voltage. Increasing P_{ex} leads to the enhancement of relative intensity of IX line, i.e. reduction of IX^T/IX ratio, at low temperatures (Figures 3.2b, 3.5b), consistent with the trion density saturation at n_B and, as a result, enhanced fraction of IXs with increased n_P.

We also briefly discuss alternative intepretations for the two lines of spatially indirect luminescence. A splitting of IX or DX emission to two luminescence lines is a general phenomenon in two coupled TMD layers. Various interpretations based on the assignment of the lines to different states of neutral excitons were offered to explain this splitting: The interpretations in terms of (i) excitonic states split due to the CB K-valley spin splitting [47], (ii) excitonic states indirect in momentum space and split due to the valley energy difference [76,83]

or spin-orbit coupling [84], and (iii) excitonic states in moiré superlattice [86–89,91,92] following the theory of moiré IXs and DXs [44,45,93].

However, interpretations based on different states of neutral excitons, including interpretations (i)-(iii) outlined above, do not offer a good agreement with the experimental data in Figure 3.5 and, in turn, a plausible explanation for the IX lines in the studied heterostructures. As detailed in section 3.6, for different states of neutral excitons, the relative occupation of the lower-energy state and, as a result, the relative intensity of the lower-energy line should increase by orders of magnitude with lowering the temperature in the range $1/T = 0.03 - 0.6\ 1/\mathrm{K}$ (Figure 3.12). However, the experimental data (Figures 3.5, 3.10, and 3.12) show the nearly constant relative intensity of the lower-energy line in this temperature range. In contrast, the theory of neutral excitons and trions is in agreement with the data (Figures 3.5, 3.10, and 3.12). The large discrepancy, by orders of magnitude, between the interpretations of the two indirect luminescence lines based on two different states of neutral IXs and the experimental data, indicates that these interpretations are less plausible than the interpretation based on neutral exciton IX and trion IX^T that is in agreement with the data (Figures 3.5, 3.10, and 3.12).

3.3 Luminescence Maps

The spatially indirect (interlayer) luminescence intensity is enhanced at the bright spots (sample S: Figure 3.2a and Figure 3.6a; sample M: Figure 3.7a). Both in sample S and sample M, the bright spots are observed close to the flake boundary (Figures 3.6a and 3.7a). In contrast, the spatially direct (intralayer) luminescence intensity varies only slightly in the CQW heterostructures and does not show an intensity enhancement in the bright spots (sample S: Figure 3.6b,c; sample M: Figure 3.7b).

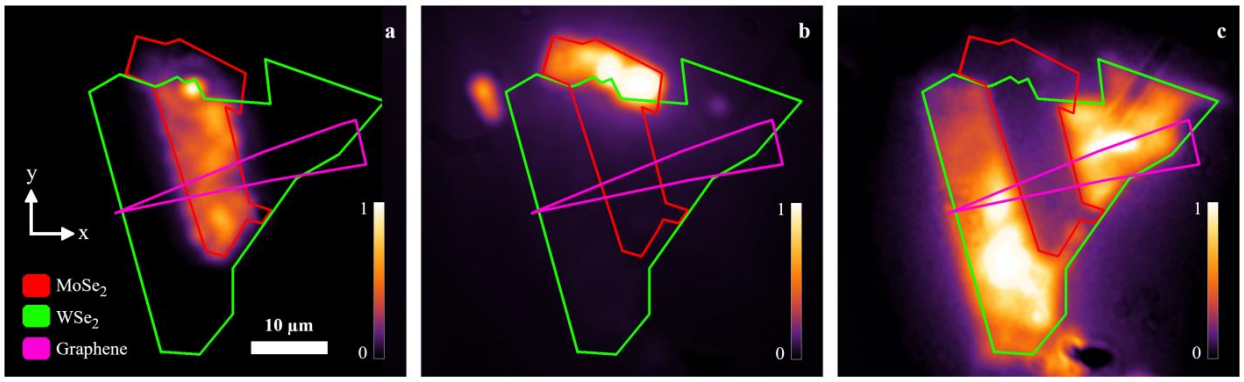

Figure 3.6: Sample S luminescence maps. x-y luminescence image of (a) the spatially indirect (interlayer) luminescence (measured in the spectral range 1.24–1.46 eV) and (b,c) the spatially direct (intralayer) luminescence in (b) $MoSe_2$ (measured in the spectral range 1.60–1.62eV eV) and (c) WSe_2 (measured in the spectral range 1.66–1.69eV eV) in sample S. The layer boundaries are shown. Laser excitation is defocused. $\boldsymbol{V_g}$ = 0, T = 1.7 K

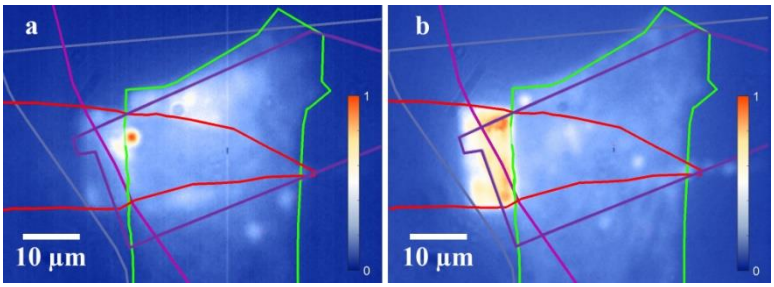

Figure 3.7: Sample M luminescence maps. x-y luminescence image of (a) the spatially indirect (interlayer) luminescence (measured in the spectral range 1.24–1.4 eV) and (b) the spatially direct (intralayer) luminescence (dominating in the spectral range 1.24–1.91 eV) in sample M. The layer boundaries are shown. Laser excitation is defocused. $\boldsymbol{V_g}$ = 0, T = 1.7 K.

The bright spots show up to an order of magnitude enhancement of IX luminescence intensity in comparison to the surrounding region of the CQW heterostructure (Figure 3.7a). The IX luminescence in the bright spot is localized within ~ 2 µm in sample S and within the length smaller than the 1 µm resolution of the optical system used in the experiment in sample M.

3.4 Power and Voltage Dependence

The narrowest indirect luminescence linewidth is observed at the smallest excitation power P_{ex} in the experiment. With increasing P_{ex}, the indirect luminescence broadens (Figure 3.8a,d) and shifts to higher energies (Figure 3.8a,b).

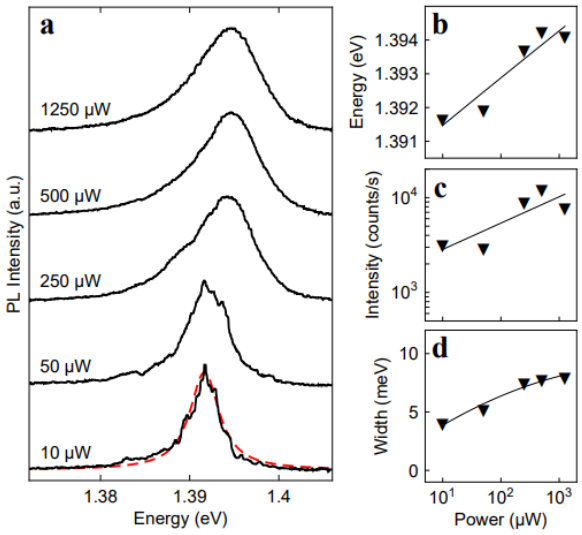

Figure 3.8: Bright spot power dependence. (a) Indirect luminescence spectra at different excitation powers $\boldsymbol{P_{ex}}$. (b-d) The peak energy (b), intensity (c), and linewidth (d) of the luminescence line in (a) vs. $\boldsymbol{P_{ex}}$. These parameters are extracted from Lorentzian fits to the luminescence lines, an example is shown for the 10 μW spectrum by a red dashed line in (a). The curves are guides to the eye. $\boldsymbol{V_g}$ = 0, T = 1.7 K.

The IX energy at the CQW flake is controlled by voltage V_g (Figures 3.3, 3.9a,b). For sample S, the bias across the CQW is applied by a narrow graphene stripe on the top of the heterostructure (Figure 3.2a) and the voltage dependence presented in Figure 3.9a is measured at the graphene stripe location. For sample M, the graphene layer covers the entire CQW flake and the voltage dependence in Figure 3.9b is measured at the flake center. With increasing V_g, the IX energy increases in sample M (Figure 3.3 and 3.9b) and reduces in sample S (Figure 3.9a), in agreement with the different order of $MoSe_2$ and WSe_2 layers in samples M and S. The neutral and charged indirect exciton peaks, IX and IX^T, are not resolved at the CQW flake in sample M due to larger luminescence linewidth in this region of the sample. The energy shifts with voltage in the CQW flake (Figure 3.9b) and bright spot (Figure 3.3) are roughly the same, indicating that in both these regions the indirect luminescence lines correspond to IXs with the same d_z.

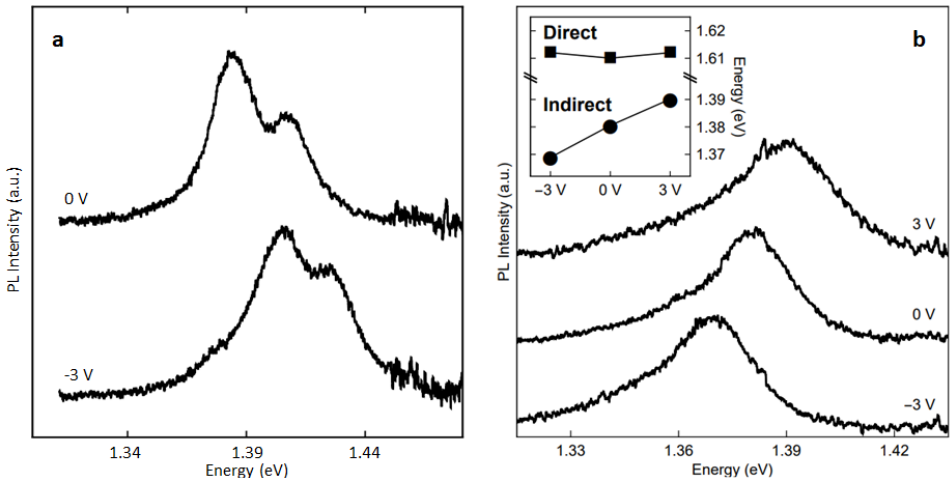

Figure 3.9: CQW flake gate voltage dependence. (a) Indirect luminescence spectra at the CQW flake in sample S (a) and M (b) at different gate voltages $\boldsymbol{V_g}$. The neutral and charged indirect exciton peaks, IX and IX^T, are not resolved in (b) due to larger luminescence linewidth in this region of the sample. The inset in (b) shows the peak energy of direct and indirect luminescence lines vs. $\boldsymbol{V_g}$. $\boldsymbol{P_{ex}}$ = 3.4 (a) and 1.25 (b) mW. T = 1.7 K.

3.5 Temperature Dependence of Sample S

Temperature dependences of luminescence at the CQW flake (Figures 3.4a and 3.5b repeated in Figures 3.10b and 3.10e) and at the bright spot (Figure 3.10d,f) in sample S are similar. Similar temperature dependences are also observed for low (Figure 3.10a,c) and high (Figure 3.10b,d) excitation powers. With reducing temperature, the luminescence intensity ratio of the lines IX^T/IX increases at high temperatures and saturates at low temperatures (Fig3.10a-d and symbols at Figure 3.10e,f) in agreement with the mass action law for the indirect trions (blue and green lines in Figure 3.10e,f).

3.6 Simulations

The simulations set off with determining the densities of excitons and trions from the mass action model following [118]. The mass of an exciton is $m_X = m_e + m_h$ and that of a trion

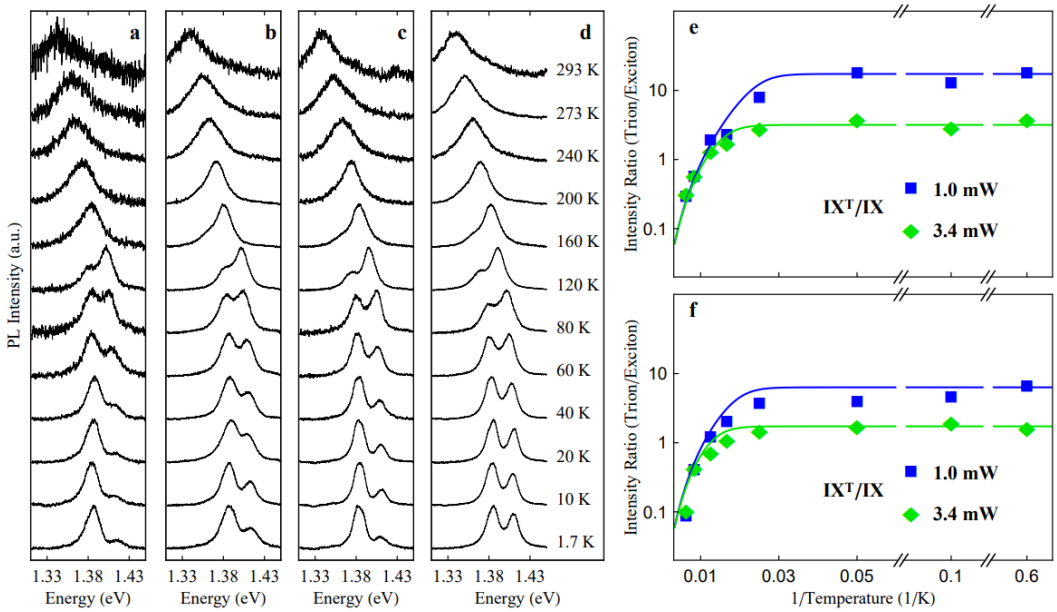

Figure 3.10: Extended temperature dependence. (a-d) Indirect luminescence spectra at the CQW flake (a,b) and at the CQW bright spot (c,d) at different temperatures. Excitation power $\boldsymbol{P_{ex}}$ = 1 mW (a,c) and 3.4 mW (b,d). (e,f) Experimental (symbols) and simulated (lines) spectrally integrated luminescence intensity ratio IX^T/IX vs. 1/temperature at the CQW flake (e) and at the CQW bright spot (f). $\boldsymbol{P_{ex}}$ = 1 mW (blue squares) and 3.4 mW (green diamonds), $\boldsymbol{V_g}$.

is $m_T = 2m_e + m_h$. The densities of excitons n_X, trions n_T, and free electrons n_e are determined from conditions

$$n_P = n_X + n_T$$

$$n_B = n_T + n_e$$

$$n_X\, n_e / n_T = A k_B T exp\left(-\frac{E_T}{k_B T}\right)$$

where k_B is the Boltzmann constant, T is the ambient temperature, n_B is the density of background charge carriers, n_P is the density of photoexcited electron-hole pairs, E_T is the trion binding energy, and $A = (4m_e m_X)/(\pi\hbar^2 m_T)$. The trion binding energy is taken from the measured line splitting: E_T = 28 meV for indirect trion in sample S and 26 meV for indirect trion in sample M and E_T = 32 meV for direct trion in $MoSe_2$ (Figure 3.4). This model gives the ratio of exciton and trion densities presented in Figure 3.5 and 3.10 by black (for direct exciton and

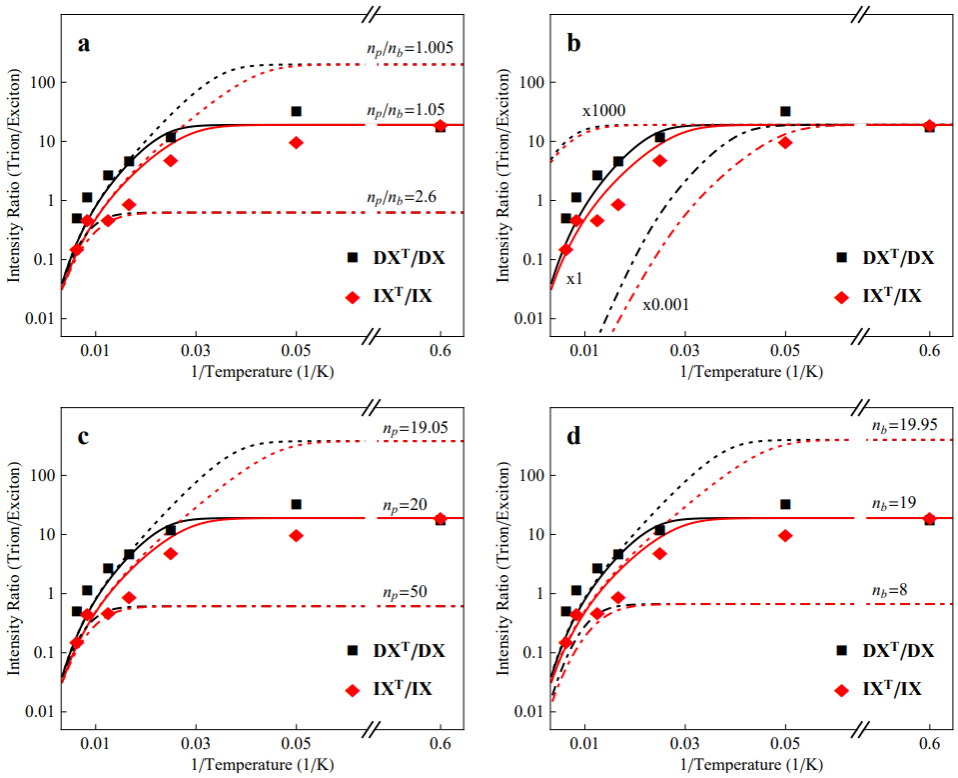

Figure 3.11: Trion/exciton simulations. The measured (symbols) and simulated (lines) spectrally integrated luminescence intensity ratio IX^T/IX (red) and DX^T/DX (black) vs. 1/temperature (a) for fixed $\boldsymbol{n_B = 1.9 \times 10^{11}\ cm^{-2}}$ fitted to the high-temperature data and different $\boldsymbol{n_P/n_B}$, (b) for fixed $\boldsymbol{n_P/n_B = 1.05}$ fitted to the low-temperature data and different $\boldsymbol{n_B}$ (solid lines for $\boldsymbol{n_B = 1.9 \times 10^{11}\ cm^{-2}}$, dotted and dashed-dotted lines for 1000 times higher and lower $\boldsymbol{n_B}$, respectively), (c) for fixed $\boldsymbol{n_B = 1.9 \times 10^{11}\ cm^{-2}}$ and different $\boldsymbol{n_P}$, (d) for fixed $\boldsymbol{n_P = 2 \times 10^{11}\ cm^{-2}}$ and different $\boldsymbol{n_B}$. The densities indicated in the figure are in $\boldsymbol{10^{10}\ cm^{-2}}$.

trion) and red, green, and blue (for indirect exciton and trion) lines.

The simulations give qualitatively similar results for various n_P and n_B: At high temperatures, the ratio n_T/n_X increases with reducing temperature, however, at low temperatures, n_T/n_X saturates (Figure 3.11). This saturation is the key characteristic of trion luminescence.

An estimate for n_P and n_B can be obtained by treating them as fitting parameters (Figure 3.11). The procedure of estimating n_P and n_B is simplified by separate fitting of the ratio n_P/n_B and then n_B (or n_P) to the low- and high-temperature data, respectively, as described below. In the limit of vanishing temperatures, equations (1)–(3) give the expected result: the trion density

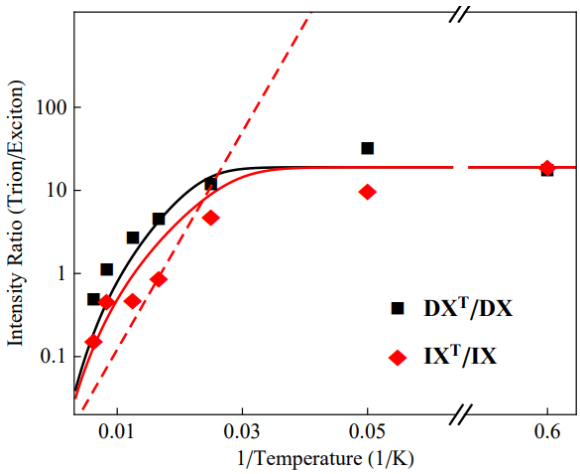

Figure 3.12: Comparison with two states of neutral IXs. The measured (symbols) and simulated (solid lines) spectrally integrated luminescence intensity ratio IX^T/IX (red) and DX^T/DX (black) vs. 1/ temperature (same data as in Figure 3.5a). The simulation of the indirect trion IX^T to indirect neutral exciton IX line intensity ratio (solid red line) is in agreement with the experiment (red symbols). Exponential ratio $\boldsymbol{exp(\Delta E/k_B T)}$ for two states of neutral IXs separated by $\boldsymbol{\Delta E}$ = 26 meV (red dashed line) does not offer a good agreement with the experiment.

saturates at n_B and, in turn, the ratio n_T/n_X asymptotically approaches $n_B/(n_P - n_B) = 1/(n_P/n_B - 1)$. Therefore fitting the low-temperature data gives an estimate for n_P/n_B (Figure 3.11a). Then n_B and, in turn, n_P can be estimated by fitting the high-temperature data (Figure 3.11b). The obtained fitting parameters for sample M are $n_B = 1.9 \times 10^{11}$ cm^{-2} and $n_P = 2 \times 10^{11}$ cm^{-2}. Figures 3.11c and 3.11d show the variation of n_T/n_X with n_P and n_B, respectively.

Figure 3.12 reproduces the measured (symbols) and simulated (solid lines) spectrally integrated line luminescence intensity ratio IX^T/IX (red) and DX^T/DX (black) vs. 1/temperature (same data as in Figure 3.5a). The simulation of the indirect trion IX^T to indirect neutral exciton IX line intensity ratio (solid red line) is in agreement with the experiment (red symbols) as outlined above.

We also consider alternative interpretations for the two indirect luminescence lines. In Figure 3.12, the measured temperature dependence of the line intensity ratio (Figure 3.12 symbols) is also compared with the ratio expected for different states of neutral IXs. As for the

model of a trion and a neutral exciton outlined above, we consider the states at thermal equilibrium and obeying the Maxwell-Boltzmann distribution. Thermal equilibrium is facilitated by the long IX lifetimes.

The exciton luminescence intensity is given by $n_{\mathrm{X}}/\tau_{\mathrm{r}}$ so the luminescence intensity ratio for two states of neutral IXs is given by $n_{\mathrm{X1}}/n_{\mathrm{X2}} \cdot \tau_{\mathrm{r2}}/\tau_{\mathrm{r1}} = n_{\mathrm{X1}}/n_{\mathrm{X2}} \cdot R$, where R is the ratio of radiative lifetimes τ_{r2} and τ_{r1} of the two excitonic transitions. For the splitting between two states of neutral IXs ΔE = 26 meV corresponding to the measured splitting between the lines, their luminescence intensity ratio is proportional to their occupation ratio $exp(\Delta E/k_{\mathrm{B}}T)$ shown in Figure 3.12 by red dashed line. Treating R as an adjustable parameter for achieving as good as possible agreement with the experiment allows shifting the red dashed line vertically keeping its slope unchanged in Figure 3.12. For the red dashed line in Figure 3.12, R ~ 150 (with the higher energy exciton state having 150 times shorter radiative lifetime than the lower energy exciton state) to fit the experimental point at T = 60 K, this provides a better fit to the experiment, however, assuming other R does not change the discussion below. [For a model based on two states of neutral IXs, an explanation of the higher intensity of the higher energy exciton line observed at T > 60 K (Figures 3.4 and 3.10) requires a significantly higher oscillator strength for the higher energy exciton state.] Figure 3.12 shows that $exp(\Delta E/k_{\mathrm{B}}T)$ (red dashed line) does not agree with the experimental data. Since varying the ratio R of radiative lifetimes of the two excitonic transitions only moves the dashed line vertically in Figure 3.12, no agreement is achieved for any R. For instance, in the range T = 20 – 160 K the measured intensity ratio drops by ~ 50 times while the intensity ratio for two states of neutral IXs $exp(\Delta E/k_{\mathrm{B}}T)$ drops by 5×10^5 times (Figure 3.12). This large discrepancy, by orders of magnitude, indicates that interpretations of the two indirect luminescence lines based on two different states of neutral IXs

are less plausible than the interpretation based on neutral exciton IX and trion IX^T, which is in agreement with the data.

The recombination kinetics of both excitons and trions can change with temperature [124–126] and these changes can affect the ratio of the exciton and trion luminescence intensities. However, these changes appear to be small enough to cause no qualitative change of the temperature dependence for the trion/exciton luminescence intensity ratio as evidenced by the data for direct excitons and trions which follow the mass action law [118]. Similarly, the data for both direct excitons and trions (Figure 3.5) and indirect excitons and trions (Figures 3.5, 3.10) follow the mass action law in our work.

The relative occupation of two exciton states (including neutral and charged excitons) is determined, in particular, by the decay rate and energy relaxation rate. For the case of long lifetimes, when the decay is long compared to the energy relaxation, the relative occupation approaches the thermal equilibrium. Even for direct excitons and trions characterized by short lifetimes the trion/exciton luminescence intensity ratio follows the thermal equilibrium mass action law (Ref. [118] and data in Figure 3.5 for direct excitons and trions in our work). For indirect excitons and trions, the decay is orders of magnitude slower than for direct, so they can approach the thermal equilibrium significantly better than direct. Since direct excitons and trions and indirect excitons and trions have different degree of thermal equilibrium yet similarly follow the mass action law with the saturation of trion/exciton luminescence intensity ratio at low temperatures, the saturation is not caused by the lack of thermal equilibrium. Otherwise, the deviation from the thermal equilibrium mass action law would be substantially different for DX^T/DX and IX^T/IX luminescence intensity ratio that is not the case (Figures 3.5, 3.10).

3.7 Conclusion and Outlook

In conclusion, we present studies of $MoSe_2/WSe_2$ heterostructures and report on two lines of spatially indirect luminescence whose energy splitting and temperature dependence identify them as neutral indirect excitons and charged indirect excitons, i.e. indirect trions. The identification of the two lines as neutral and charged IXs has implications on the observation of IX condensation in TMD heterostructures. Since a charged IX has more fermionic character (due to the addition of an extra electron), it may not be possible to observe Bose-Einstein condensation in a system of indirect trions. Precise control of the charge density in the system by addition of an electrode attached to the TMD monolayers may enable realization of a purely neutral IX state that facilitates the observation of IX condensation. However, this does not preclude the possibility of condensation within the neutral IX state, if the photoexcited carrier density is sufficiently high that all background charge carriers are already bound into trions.

3.8 Acknowledgements

The text of chapter 3, in part, is a reprint of the material as it appears in E. V. Calman, L. H. Fowler-Gerace, D. J. Choksy, L. V. Butov, D. E. Nikonov, I. A. Young, S. Hu, A. Mischenko, and A. K. Geim, Indirect Excitons and Trions in $MoSe_2/WSe_2$ van der Waals Heterostructures. *Nano Lett*. 20, 1869 (2020). © American Chemical Society, where the dissertation author is the co-first author. The co-authors in these publications directed, supervised, and co-worked on the research which forms the basis of this chapter.

Chapter 4

Voltage-Controlled IX Propagation

4.1 Introduction

Spatially indirect excitons (IXs) are formed by electrons and holes confined in separated layers. The separation between the electron and hole layers allows for controlling the overlap of electron and hole wave functions and achieving long IX lifetimes, orders of magnitude longer than lifetimes of spatially direct excitons (DXs) [9]. The long IX lifetimes allow them to travel over long distances before recombination [13,19,20,24,68,69,127–130].

IXs have built-in dipole moments ed_z (d_z is the separation between the electron and hole layers) and their energy can be controlled by voltage: Gate voltage V_g controls the electric field normal to the layers $F_z \propto V_g$ and changes the IX energy by ed_zF_z. This allows for creating tailored in-plane potential landscapes for IXs $\delta E(x,y) = -ed_zF_z(x,y)$ and controlling them *in situ* by voltage $V_g(x,y)$. The possibility to control IX energy by voltage and the ability of IXs to propagate over long distances led to the realization of a variety of tailored voltage-controlled in-plane potential landscapes, which are explored in studies of IX transport. These landscapes include excitonic ramps [20,68], excitonic lattices [18,131,132], excitonic narrow channels [133,134], excitonic conveyers [22], and excitonic split gate devices [135].

IX devices are also explored for developing signal processing based on the exciton dipole, that is a novel computational state variable, different from established computational state variables such as electron charge in electronic devices. Potential advantages of excitonic devices

include energy-efficient signal processing and seamless coupling to optical communication [19]. Experimental proof-of-principle was demonstrated for excitonic transistors [25,70].

The realization of excitonic devices, whose operation is based on controlled propagation of excitons, relies on meeting the requirements of (i) long-range IX propagation over lengths exceeding the in-plane dimensions of excitonic devices and (ii) in situ control of IX propagation, in particular, by voltage. These requirements were met with IXs in GaAs heterostructures and the studies outlined above used the GaAs platform.

However, excitons exist at temperatures roughly below $E_{\mathrm{Ry,IX}}/k_{\mathrm{B}}$ (E_{ex} the exciton binding energy, k_{B} the Boltzmann constant) [26] and, due to their low binding energies, IXs in GaAs heterostructures exist at low temperatures. $E_{\mathrm{Ry,IX}}$ is typically 4 meV in GaAs/AlGaAs heterostructures [27] and achieves 10 meV in GaAs/AlAs heterostructures [28]. The proof of principle for the operation of IX switching devices based on voltage-controlled IX propagation was demonstrated up to ~ 100 K in GaAs heterostructures [70]. IX devices based on controlled IX propagation are also explored in GaN/AlGaN heterostructures with high $E_{\mathrm{Ry,IX}}$ reaching ~ 30 meV [73].

Van der Waals heterostructures composed of atomically thin layers of TMD [31] allow the realization of excitons with high binding energies [74,75]. IXs in TMD heterostructures are characterized by binding energies reaching hundreds of meV [37,38] making them stable at room temperature [49]. Due to the high IX binding energy, TMD heterostructures can form a material platform for creating excitonic devices operating at high temperatures suitable for applications.

However, in contrast to GaAs heterostructures, a characteristic feature of TMD heterostructures is the presence of significant moiré superlattice potentials, which are predicted to cause modulations of IX energy reaching tens of meV in mechanically stacked TMD

heterostructures with adjacent electron and hole layers and a small angle $\delta\theta$ between the layers, such as the studied $MoSe_2/WSe_2$ heterostructure. Strong variations of the interlayer band gap within the moiré supercell, Δ, causing the modulations of IX energy were predicted for these TMD heterostructures with both R (AA, 0° twist) and H (AB, 60° twist) stacking Δ 100 (90) and 25 (17) meV for $MoSe_2/WSe_2$ heterobilayers with R and H stacking, respectively, in Ref. [45] (in Ref. [44]). Large Δ were also predicted for other TMD heterostructures of this type [44,45]. A spatial modulation of the local bandgap with an amplitude of 150 meV was reported in scanning tunneling microscopy measurements and calculations of a rotationally aligned MoS_2/WSe_2 hetero-bilayer [42]. The moiré superlattice period $b \sim a/\sqrt{\delta\theta^2 + \delta\phi^2}$ is typically in the ca. 10 nm range (a is the lattice constant, $\delta\phi$ is the lattice mismatch, $\delta\theta$ is the twist angle deviation from $m\pi/3$, m is an integer) [136,137].

This prediction inspired extensive experimental studies. For instance, the moiré superlattices were considered as the origin of splitting of IX luminescence to two or more lines [86–92]. In these works, the strong modulations of IX energy in the moiré potentials were, in particular, evidenced by wide spreads of luminescence line energies of excitons localized in the moiré potential minima. Four (five) luminescence lines spread over ~ 70 (100) meV in $MoSe_2/WSe_2$ with 1° (2°) twist were discussed in terms of exciton states localized in a moiré potential of ~ 150 meV [88]. Multiple narrow luminescence lines were spread over ~ 30 meV in $MoSe_2/WSe_2$ with 2° twist and ~ 20 (30) meV in $MoSe_2/WSe_2$ with 60° (56°) twist [89]. WSe_2 absorption resonances spread over ~ 100 meV in both R- and H-stacked WSe_2/WS_2 were discussed in terms of a peak-to-peak exciton moiré potential of 250 meV [92].

We note however that there are other interpretations of the splitting of IX luminescence line, including excitonic states split due to the conduction band K-valley spin splitting [47],

excitonic states indirect in momentum space and split due to the valley energy difference [76,83] or spin-orbit coupling [84], and neutral and charged IX states [138]. We considered the origin of splitting of IX luminescence to two lines in Ref. [138].

The predicted strong moiré superlattice potentials in TMD heterostructures should have a significant effect on exciton propagation. The strong in-plane energy landscapes can lead to IX localization, making IX propagation fundamentally different in TMD and GaAs heterostructures and making uncertain if long-range IX propagation can be realized in principle in TMD heterostructures with moiré superlattice potentials.

Propagation of both DXs in TMD monolayers [139–144] and IXs in TMD heterostructures [50–55] is intensively studied. A relatively short-range IX propagation with $1/e$ luminescence decay distances reaching ~ 3 μm [50,51,53–55], control of IX propagation by voltage within these distances [53,54], and control of DX luminescence by voltage up to 5 μm away from the generation spot [52] were reported in TMD heterostructures.

The extent to which the moiré superlattice potentials affect the IX diffusivity is not fully established. The comparison of $MoSe_2/WSe_2$ heterostructures with $MoSe_2$/hBN/WSe_2 heterostructures, where the moiré superlattice potential is suppressed by an hBN spacer between the $MoSe_2$ and WSe_2 layers, evidences the reduction of IX propagation due to moiré superlattice potentials: the IX propagation with the $1/e$ decay distance up to 2.6 μm was observed in $MoSe_2$/hBN/WSe_2 and shorter IX propagation with the $1/e$ decay distance beyond the laser spot below 1 μm was observed in $MoSe_2/WSe_2$ [53].

We realize in a $MoSe_2/WSe_2$ TMD heterostructure IX propagation with the $1/e$ IX luminescence decay distance $d_{1/e}$ ~ 13 μm. This long propagation distance exceeds $d_{1/e}$ ~ 3 μm realized in the earlier studies of TMD heterostructures [50,51,53–55] and is sufficiently long to

allow for creating elaborate excitonic devices and circuits within the IX propagation length that is required for performing operations with IX fluxes [25,70]. In the presented TMD materials, the long-range IX propagation occurs up to ~ 50 K. This is a step toward the room temperature operation, which can be realized in TMD heterostructures due to the high IX binding energy. We also realize control of the long-range IX propagation by voltage. The control of the IX propagation in the $MoSe_2/WSe_2$ heterostructure is governed by new mechanisms, beyond the known mechanism for controlling IX transport by an energy barrier to IX propagation (or a trap for IXs) created by the gate electrode that was reported in the studies of GaAs [25,70] and TMD [53,54] heterostructures. We discuss the origin of the voltage-controlled long-range IX propagation in the $MoSe_2/WSe_2$ heterostructure, in particular, the electric-field control of the moiré potential. The control of moiré superlattice potentials by voltage can be used in various applications ranging from excitonic devices outlined in this work to quantum simulators and quantum emitter arrays based on moiré superlattices [45,145,146].

4.2 Experiment

The $MoSe_2/WSe_2$ heterostructure is assembled by stacking mechanically exfoliated 2D crystals on a graphite substrate. The $MoSe_2$ and WSe_2 monolayers are encapsulated by hexagonal boron nitride (hBN) serving as dielectric cladding layers. The energy-band diagram is schematically shown in Figure 4.1a. IXs are formed from electrons and holes confined in adjacent $MoSe_2$ and WSe_2 monolayers, respectively. The lowest energy DX state is optically

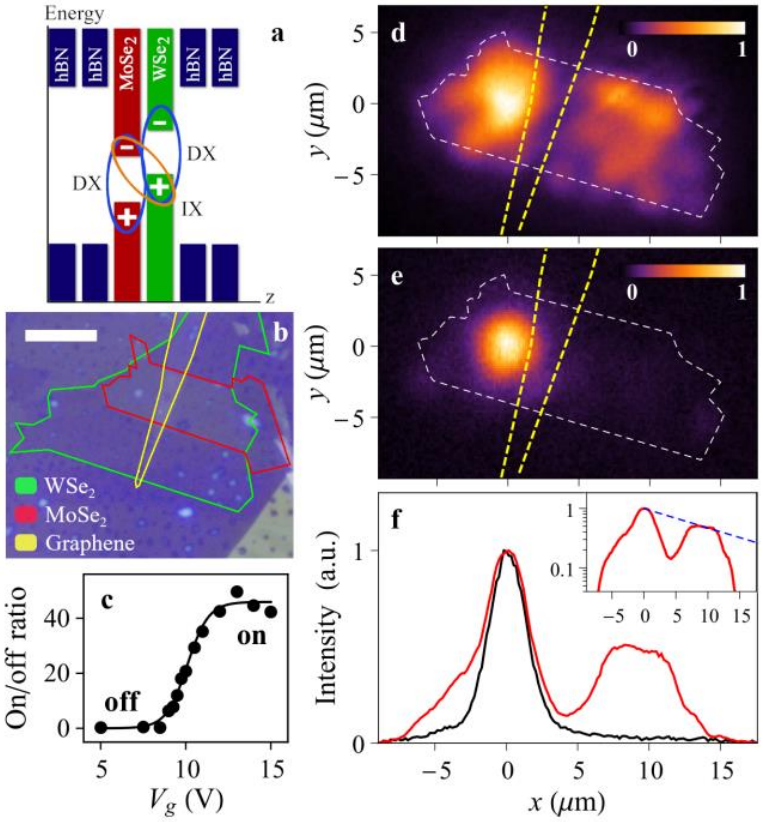

Figure 4.1: Voltage-controlled IX propagation. (a) Band diagram of van der Waals $MoSe_2/WSe_2$ heterostructure. The ovals indicate a direct exciton (DX) and an indirect exciton (IX) composed of an electron (−) and a hole (+). (b) Microscope image showing the layer pattern of the device, scale bar is 10 μm. The green, red, and yellow lines indicate the boundaries of the WSe_2 and $MoSe_2$ monolayers and graphene gate, respectively. (d,e) $\boldsymbol{x}$-$\boldsymbol{y}$ images of IX luminescence in the on (d) and off (e) state of the excitonic transistor. The white and yellow dashed lines show the boundary of the $MoSe_2/WSe_2$ heterostructure and graphene gate, respectively. The gate voltage $\boldsymbol{V_g}$ controls the IX propagation from the laser excitation spot at $\boldsymbol{x} = 0$ (the source) to the other side of the graphene gate $\boldsymbol{x} > 6$ μm (the drain). $\boldsymbol{V_g}$ = 10 V (d), 0 (e). (f) Normalized IX luminescence profiles along $\boldsymbol{y} = 0$ for the images in (d) and (e) shown by the red and black lines, respectively. Inset shows the same IX luminescence profile in the on state on log scale. For comparison, dashed line shows exponential signal reduction with $\boldsymbol{1/e}$ decay distance 13 μm. A lower IX luminescence intensity is seen in the region covered by the graphene gate, which is centered at $\boldsymbol{x} = 4$ μm. (c) Total IX luminescence intensity in the drain (integrated over $\boldsymbol{x} = 6$–13 μm) vs. $\boldsymbol{V_g}$. For all data, $\boldsymbol{P_{ex}} = 4$ mW, T = 1.7 K.

active in $MoSe_2$ and dark in WSe_2, and the lowest energy IX state is optically active [44,94,103–107]. The bias across the heterostructure is created by the gate voltage V_g applied between the narrow semitransparent multilayer graphene top gate (Figure 4.1b) and the global graphite back gate.

The graphene gate is centered at $x = 4$ μm (Figure 4.1d–f). The heterostructure region to

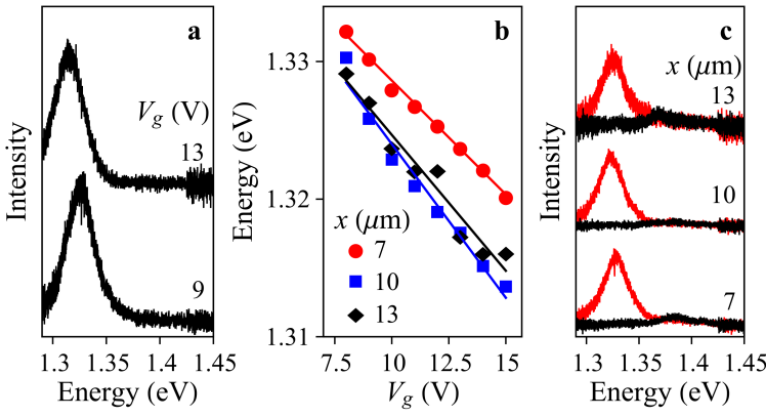

Figure 4.2: IX energy control over entire heterostructure. (a) IX luminescence spectra at $\boldsymbol{x}$ = 13 µm for gate voltages $\boldsymbol{V_g}$ = 9 and 13 V. (b) IX energy vs $\boldsymbol{V_g}$ for positions in the drain region $\boldsymbol{x}$ = 7, 10, and 13 µm. (c) IX spectra in on (red) and off (black) state of the excitonic transistor for positions in the drain region $\boldsymbol{x}$ = 7, 10, and 13 µm. $\boldsymbol{V_g}$ = 10 V (on), 8.5 V (off). For all data, $\boldsymbol{P_{ex}}$ = 4 mW, T = 1.7 K.

the left of the gate (x = -7 to 4 µm) is referred to as the source and the heterostructure region to the right of the gate (x = 6 to 13 µm) is referred to as the drain. IXs are optically generated by laser excitation focused in the source region.

When the device is in the off state, IX propagation from the source to the drain is suppressed and the IX luminescence profile follows the laser excitation profile (Figure 4.1e). When the device is switched on, IXs spread out away from the laser excitation spot and propagate to the drain region (Figure 4.1d).

Figure 4.1f shows IX luminescence profiles along y = 0 for the images in Figure 4.1d,e. Inset shows the same IX luminescence profile for the on state on log scale. For comparison, dashed line shows exponential signal reduction with the $1/e$ decay distance 13 µm. A lower IX luminescence intensity is seen in the region covered by the graphene gate. The total IX luminescence intensity in the drain region (integrated over x = 6–13 µm) increases by 40 times as the gate voltage switches from off to on (Figure 4.1c). Figures 4.1c-f present voltage-controlled long-range propagation of IXs in $MoSe_2/WSe_2$ heterostructure.

Next, we verify if the propagating luminescence signal corresponds to the IX

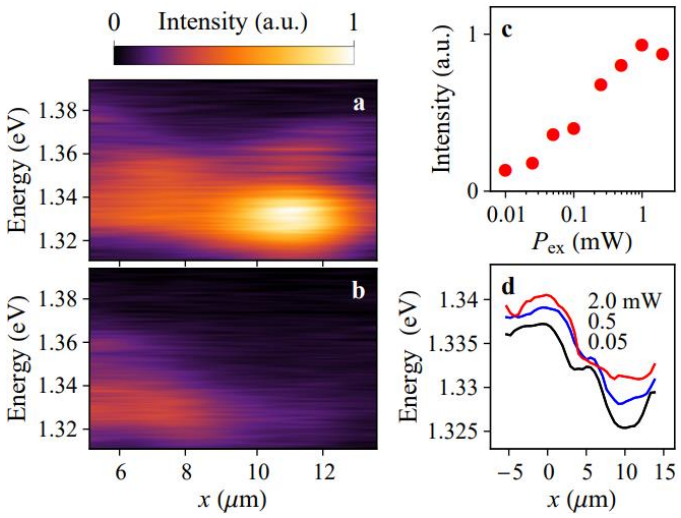

Figure 4.3: Excitation power dependence of voltage-controlled IX propagation. (a,b) $\boldsymbol{x}$-energy images of IX luminescence in the drain region for $\boldsymbol{P_{ex}}$= 2 mW (a) and 0.05 mW (b). (c) Total IX luminescence intensity in the drain (integrated over $\boldsymbol{x}$ = 6–13 μm) vs. $\boldsymbol{P_{ex}}$. (d) IX energy vs position for $\boldsymbol{P_{ex}}$ = 0.05 (black), 0.5 (blue), and 2 (red) mW. For all data, $\boldsymbol{V_g}$ = 10 V, T = 1.7 K.

luminescence. Figure 4.2a,b show that at voltages, which allow for IX propagation across the sample, the exciton luminescence energy is controlled by voltage in the entire drain region. This exhibits the basic IX property — IX energy control by voltage, outlined in the introduction. Figure 4.2c presents tracing the IX luminescence along the IX propagation path all the way up to the heterostructure edge ca. 13 μm away from the region of IX optical generation. Figure 4.2c also shows that IX luminescence spectra at the drain demonstrate effective switching behavior between the off (black spectra) and on (red spectra) state. Tracing the IX luminescence along the IX propagation path with $1/e$ IX luminescence decay distance 13 μm and controlling IX propagation by voltage present the direct measurement of long-range IX propagation and excitonic transistor action in TMD heterostructures.

The IX luminescence spectra are traced over the drain region at different excitation powers P_{ex} (Figure 4.3a,b). The total IX luminescence intensity in the drain increases with P_{ex} (Figure 4.3c). Figures 4.3a–c show that the IX propagation enhances with excitation power. Maximum IX propagation with $d_{1/e}$ ~ 13 μm is realized at P_{ex} ~ 1 mW. Comparable P_{ex} were

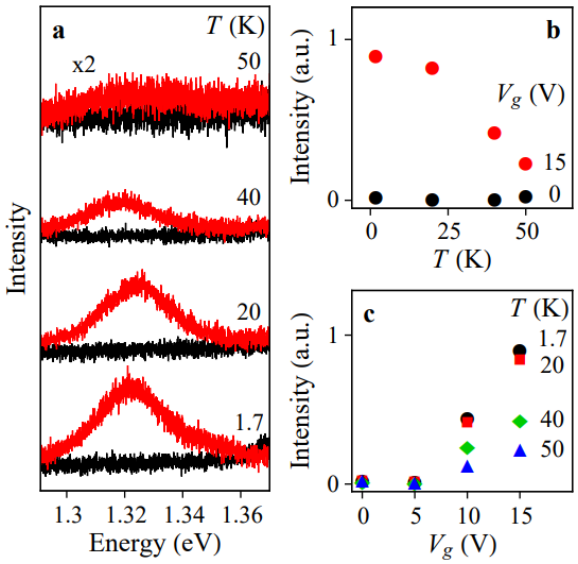

Figure 4.4: Temperature dependence of voltage-controlled propagation. (a) IX luminescence spectra in the drain at $\boldsymbol{x}$ = 13 µm at temperatures $\boldsymbol{T}$ = 1.7, 20, 40, and 50 K in on (red) and off (black) state of the excitonic transistor. $\boldsymbol{V_g}$ = 15 V (on) and 0 (off). (b) Total IX luminescence intensity in the drain (integrated over $\boldsymbol{x}$ = 6–13 µm) vs. temperature in on ($\boldsymbol{V_g}$ = 15 V) and off ($\boldsymbol{V_g}$ = 0 V) state. (c) Total IX luminescence intensity in the drain (integrated over $\boldsymbol{x}$ = 6–13 µm) vs. $\boldsymbol{V_g}$ for temperatures $\boldsymbol{T}$ = 1.7, 20, 40, and 50 K. For all data, $\boldsymbol{P_{ex}}$ = 4 mW.

explored in the studies of TMD heterostructures where $d_{1/e}$ ~ 3 µm was realized [51,53].

Figure 4.3d shows the optically measured IX energy along the IX propagation path. The overall IX energy reduction is observed (i) with increasing separation from the IX optical generation spot and (ii) with reducing P_{ex}. Both indicate a reduction of IX energy with the reduced IX density. This is consistent with the repulsive interaction between IXs, which are dipoles oriented normal to the layers. Similar reduction of IX energy with increasing separation from the optical generation spot or with reducing P_{ex} is also characteristic of IXs in GaAs heterostructures and is explained in terms of the repulsive interaction between IX dipoles [24]. The local IX energy variations in the range of a few meV (Figure 4.3d) are likely caused by the lateral potential landscape across the heterostructure. The IX energy variations due to the moiré superlattice have the period in the ca. 10 nm range [136,137], these short-range energy variations are not resolved in the optical experiment with resolution 1.5 µm.

Figure 4.4 presents the temperature dependence of IX propagation. The long-range IX propagation through the drain region and the switching between on and off state are observed up to approximately 50 K.

4.3 Discussion

The phenomenological properties of voltage-controlled long-range IX propagation in $MoSe_2/WSe_2$, outlined above, are qualitatively different from those in GaAs heterostructures [25,70]. GaAs/AlAs heterostructures, where IXs are formed from electrons and holes confined in adjacent AlAs and GaAs layers, respectively, have a staggered band alignment [28,70] similar to $MoSe_2/WSe_2$ heterostructures (Figure 4.1a). This makes GaAs/AlAs heterostructures a more close system for the comparison with $MoSe_2/WSe_2$ heterostructures. For the excitation spot positioned in the source region, similar to the experimental geometry in Figure 4.1, in the GaAs/AlAs heterostructures IX propagation is long-range at V_g while both a positive and negative voltage on a gate creating a barrier and a trap for IXs, respectively, suppress the IX propagation [70]. This behavior is opposite to the voltage-controlled IX propagation in $MoSe_2/WSe_2$ where applied voltage strongly enhances the IX propagation (Figure 4.1).

The opposite behavior is also observed for the excitation spot positioned on the gate electrode. For the GaAs/AlAs heterostructures, trapping (anti-trapping) IX potentials created by gate voltage cause the IX cloud confinement in (spreading away from) the gate region [70]. For the $MoSe_2/WSe_2$ heterostructure, the IX energy reduces with increasing V_g that facilitates trapping IXs in the gate region. However, similar to the case of excitation in the source region (Figure 4.1), an enhancement of the IX propagation away from the excitation spot with

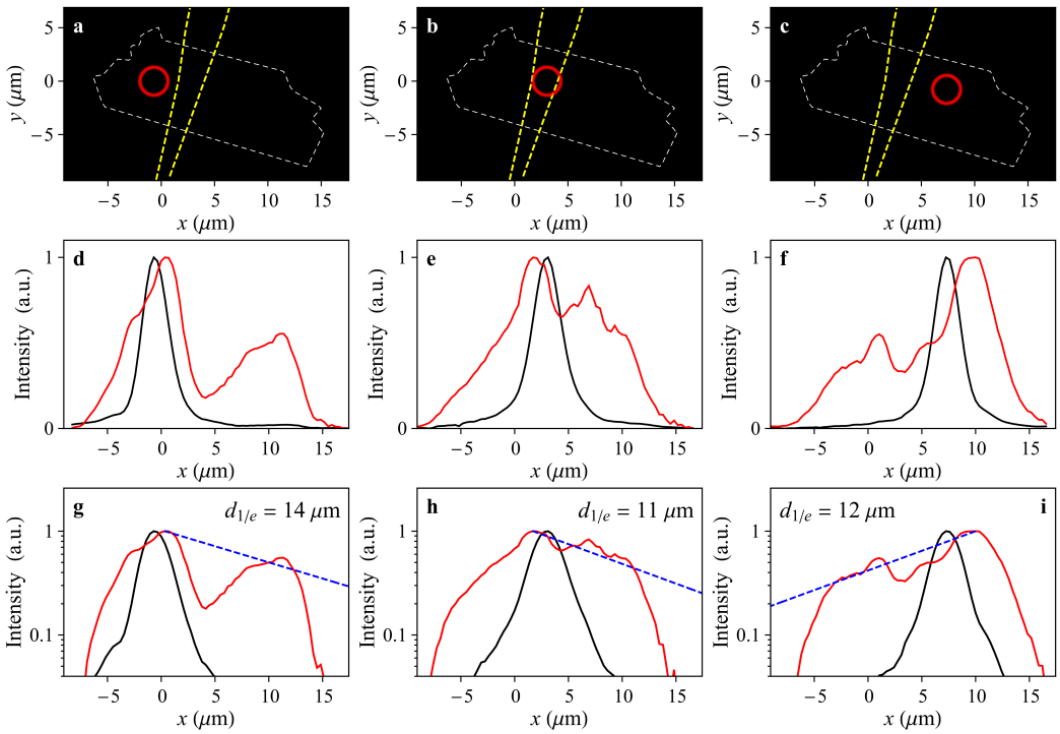

Figure 4.5: Position dependence of voltage-controlled propagation. (a-c) The white and yellow dashed lines show the boundaries of $MoSe_2/WSe_2$ heterostructure and graphene gate, respectively. The laser excitation spot [red circle in (a-c)] is positioned at the source (a,d,g), gate (b,e,h), and drain (c,f,i) region of the device. The gate voltage $\boldsymbol{V_g}$ controls the IX propagation from the laser excitation spot. (d-f) Normalized IX luminescence profiles along $\boldsymbol{y}$ = 0 for $\boldsymbol{V_g}$= 10 V (red lines) and 0 (black lines). (g-i) Same IX luminescence profiles on log scale. For comparison with the IX luminescence profiles at $\boldsymbol{V_g}$ = 10 V, dashed lines show exponential signal reduction with $\boldsymbol{1/e}$ decay distance $\boldsymbol{d_{1/e}}$ = 14, 11, and 12μm, respectively. A lower IX luminescence intensity is seen in the region covered by the graphene gate, which is centered at $\boldsymbol{x}$ = 4 μm. For all data, $\boldsymbol{P_{ex}}$ = 4 mW, T = 1.7 K.

increasing V_g is observed in the case of excitation in the gate region (Figure 4.5).

In GaAs heterostructures, the IX propagation has been controlled by an energy barrier to IX propagation (or a trap for IXs) created by the gate electrode [25,70]. The control of IX transport realized in TMD heterostructures was referred to the same mechanism [53,54]. The qualitative differences outlined above show that the IX long-range propagation in the $MoSe_2/WSe_2$ heterostructure is controlled by a new mechanism, different from the control by an energy barrier or a trap for IXs created by the gate electrode.

This new mechanism enables the long-range IX propagation away from the excitation spot not only through the gate but everywhere in the plane of the heterostructure: Figure 4.1d–f

shows that increasing V_g enables the IX propagation away from the excitation spot both through the gate (toward positive x) and in the opposite direction (toward negative x); Figure 4.5 shows that increasing V_g enables the IX propagation away from the excitation spot for any excitation spot position on the heterostructure.

The predicted strong moiré superlattice potentials [44,45,93,94] in the studied $MoSe_2/WSe_2$ heterostructure are expected to localize IXs and, therefore, the existence of the long-range IX propagation is nontrivial. Identifying the mechanism, which can lead to the voltage-controlled long-range IX propagation in the heterostructures with the predicted moiré superlattice potentials forms the challenge for theoretical investigations. The relevant experimental data and possible origin of the voltage-controlled long-range IX propagation in the $MoSe_2/WSe_2$ heterostructure are discussed below.

IXs are the lowest energy exciton state in $MoSe_2/WSe_2$ heterostructures even at no applied voltage (Figure 4.1a). The absence of long-range IX propagation at $V_g = 0$ indicates IX localization. As outlined above, the moiré superlattice potentials are predicted to cause modulations of exciton energy reaching tens of meV [44,45,93,94] and these strong energy modulations can lead to the exciton localization.

The regime of long-range IX propagation is realized at $V_g > 8$ V (Figure 4.1c,d). The applied electric field can tune the moiré potential and cause the long-range IX propagation. The theory [45] predicts that the moiré potential is tuned by voltage in both R- and H-stacked TMD heterostructures. In particular, increasing electric field can reduce the moiré potential amplitude and can energetically align the potential energy minima at different sites of the moiré supercell, thus causing percolation of IX states through the structure [45]. The tuning of the moiré potential can cause the observed long-range IX propagation with applied electric field. The calculated

electric field corresponding to the IX percolation is in the range of a few tenths of V/nm [45]. This is of the same order of magnitude with the estimated electric field for the onset of IX propagation in the studied device: V_g > 8 V creates electric field ~ 0.1 V/nm. We note however that a comparison with the theory can be complicated by factors including a possible built-in electric field [49], trion formation [138], moiré-site-dependent exciton binding energy and dipole moment [45], and atomic reconstruction, which can change the potential landscape and can create a network of propagation channels [46,147–150].

Besides the moiré potential, samples have disorder potential due to the heterostructure imperfections. The disorder potential also contributes to the IX localization and suppresses the IX propagation. The long-range IX propagation requires samples with a small disorder. The long-range propagation indicates the small disorder for IX transport scattering in the studied device.

In the regime of long-range IX propagation, V_g > 8 V, the IX energy in the drain is effectively controlled by voltage applied to the graphene electrode (Figure 4.2). This indicates that voltage applied to the graphene electrode laterally extends beyond the region of the graphene electrode over the entire heterostructure. This extension, in turn, indicates that the heterostructure acquires metallic conductivity. The metallization may contribute to screening of in-plane potential landscapes, facilitating the long-range IX propagation.

The metallization may also be related to the tuning of moiré potential by applied electric field. No intentional sample doping was done for the studied heterostructure, however, unintentional n-type doping is typical for TMD layers [62]. In the studied sample, the estimated electron concentration $n_B = 1.9 \times 10^{11}$ cm^{-2} [138]. Delocalization of electrons and/or charged IXs due to the tuning of moiré potential by electric field can cause the metallization.

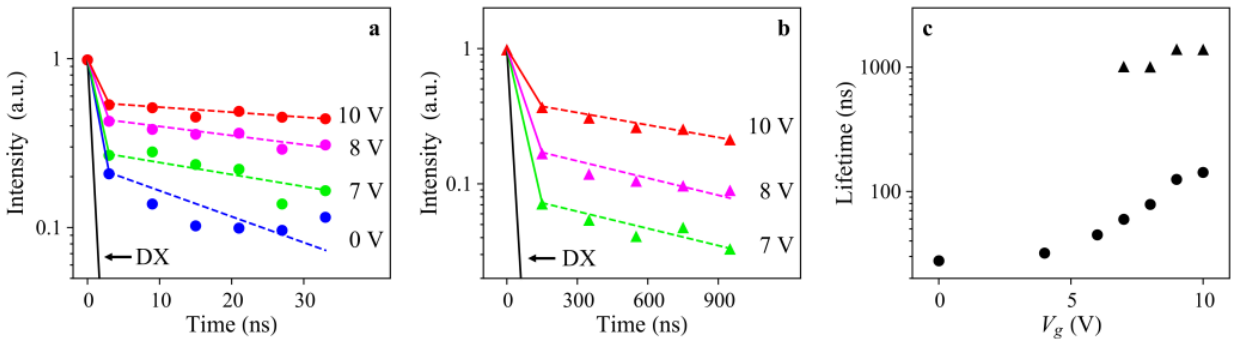

Figure 4.6: Luminescence decay of voltage-controlled propagation. (a,b) Decay of IX luminescence measured at the IX line energies 1.24–1.38 eV at short (a) and long (b) delay times vs. voltage. This energy range corresponds to the IX state showing the long-range propagation (Figure 4.2). For the data in (a), the laser excitation pulse duration $\boldsymbol{\tau_{pulse}}$ = 14 ns, period $\boldsymbol{\tau_{period}}$ = 60 ns, and edge sharpness ~ 5 ns and the signal integration window $\boldsymbol{\tau_w}$ = 6 ns. For the data in (b), to access the long delay times $\boldsymbol{\tau_{pulse}}$, $\boldsymbol{\tau_{period}}$, and $\boldsymbol{\tau_w}$ are increased to 400, 1600, and 200 ns, respectively. (c) IX luminescence decay times at short (points) and long (triangles) delay times derived from the data (a) and (b), respectively. The IX luminescence is integrated over the entire heterostructure to increase the signal. For all data, $\boldsymbol{P_{ex}}$ = 4 mW, T = 1.7 K.

The IX propagation is enhanced at higher excitation powers (Figure 4.3a–c). A similar behavior is observed for IXs in GaAs heterostructures [24]. IXs are out-of-plane dipoles, which interact repulsively. The repulsive interaction between IXs contributes to screening of in-plane potential landscapes. Furthermore, due to the repulsive interaction, the IX energy increases with density and, as a result, is higher in the region of IX generation (Figure 4.3d). This results in IX drift away from the excitation region. Both enhanced screening of in-plane potentials and drift enhance the IX propagation with increasing density [24].

Increasing V_g also increases the IX lifetime (Figure 4.6). The increase of IX lifetime contributes to the enhancement of IX propagation with voltage. The IX effective diffusion coefficient D^* can be estimated from the IX propagation length l and IX lifetime τ as $D^* \sim l^2/\tau$. For l ~ 10 μm corresponding to the IX propagation length (Figure 4.1) and τ ~ 1 μs corresponding to the IX luminescence decay time at long delay times (Figure 4.6) at V_g = 10 V, the estimate gives D^* ~ 1 cm^2/s.

The IX luminescence decay time increase with V_g is in accord with the reduction of IX

energy (Figure 4.2b) further below the DX energy that reduces the overlap of the electron and hole wavefunctions for IXs [28]. The IX decay times are orders of magnitude longer than the DX decay times [151] and are controlled by gate voltage (Figure 4.6). Different factors may contribute to deviations of the luminescence decay from an exponential decay. For instance, due to a possible heterostructure inhomogeneity the areas with shorter exciton lifetimes may contribute more at initial decay times. A fast initial component may also appear due to the decay of low-energy DX states, which appear in the IX spectral range due to the tail of DX density of states. Localized DXs at low energies in the spectral range of IXs were studied in GaAs/AlAs heterostructure [152].

4.4 Conclusions and Outlook

In summary, we realize long-range IX propagation with the $1/e$ IX luminescence decay distances reaching 13 microns in a $MoSe_2/WSe_2$ heterostructure. This propagation distance is sufficiently long to allow for creating elaborate excitonic devices and circuits. We also realize control of the long-range IX propagation by gate voltage. The control of the IX propagation in the $MoSe_2/WSe_2$ heterostructure is governed by new mechanisms, beyond the known mechanism for controlling IX transport by an energy barrier to IX propagation (or a trap for IXs) created by the gate electrode that was reported in GaAs and TMD heterostructures. We discuss the origin of the voltage-controlled long-range IX propagation in the $MoSe_2/WSe_2$ heterostructure, in particular, the electric-field control of the moiré potential.

This work presents the proof of principle to overcome moiré superlattice potentials and realize the long-range IX propagation in $MoSe_2/WSe_2$ TMD heterostructures that make TMD a promising materials platform for the development of excitonic devices. The IX binding energies

are high enough to make the IXs stable at room temperature and IXs in the laser excitation spot are observed at room temperature in $MoSe_2/WSe_2$ heterostructures [138]. However, the long-range IX propagation and the switching between the on and off state are observed up to ~ 50 K in the studied heterostructure (Figure 4.4), presumably due to the heterostructure imperfections. The realization of long-range IX propagation at higher temperatures is the subject for future works.

4.5 Acknowledgements

The text of chapter 4, in part, is a reprint of the material as it appears in L. H. Fowler-Gerace, D. J. Choksy, and L. V. Butov, Voltage-controlled long-range propagation of indirect excitons in a van der Waals heterostructure. *Phys. Rev. B*, 104, 165302 (2021). © American Physical Society, where the dissertation author is the first author. The co-authors in these publications directed, supervised, and co-worked on the research which forms the basis of this chapter.

Chapter 5

Quantum Transport of Indirect Excitons

5.1 Introduction

A spatially indirect exciton (IX) is a bound pair of an electron and a hole confined in separated layers [9]. Due to the spatial separation of electrons and holes, the lifetimes of IXs can exceed the lifetimes of spatially direct excitons (DXs) by orders of magnitude. The long lifetimes allow IXs to travel long distances before recombination. The long-range IX transport has been extensively studied in GaAs heterostructures where the $1/e$ distances of IX luminescence $d_{1/e}$ reach tens and hundreds of microns [11,13,15,18–20,22,24,25,66–69,110,127,128,130,133,153–155]. The long IX propagation distances in GaAs heterostructures allowed uncovering a number of exciton transport phenomena, including the inner ring in exciton emission patterns [13,24], the exciton localization-delocalization transition in random [13], periodic [18], and moving [22] potentials, the transistor effect for excitons [25], the long-range coherent spin transport [14,66,67], and the dissipationless exciton transport over long times evidencing the exciton superfluidity [15].

Excitons exist at temperatures roughly below $E_{\mathrm{Ry,IX}}/k_{\mathrm{B}}$ ($E_{\mathrm{Ry,IX}}$ is the exciton binding energy, k_{B} the Boltzmann constant) [26]. IXs in GaAs heterostructures exist at low temperatures due to their low binding energies: The IX binding energy is typically ~ 4 meV in GaAs/AlGaAs heterostructures [27] and ~ 10 meV in GaAs/AlAs heterostructures [28]. Furthermore, the temperature of quantum degeneracy, which can be achieved with increasing density before

excitons dissociate to electron-hole plasma, scales proportionally to $E_{\mathrm{Ry,IX}}$ [38]. Therefore, material systems where IXs have high binding energies can provide the platform for the realization of both high-temperature excitonic quantum phenomena and high-temperature excitonic devices. IXs are explored in III-V and II-VI semiconductor heterostructures based on GaAs [11,13–15,18–20,22,24,25,66–69,127,128,130,133,153–155], GaN [71–73,156], and ZnO [29,157]. Among these materials, the highest IX binding energy ~ 30 meV is in ZnO heterostructures [29].

Excitons with remarkably high binding energies can be realized in van der Waals heterostructures composed of atomically thin layers of transition-metal dichalcogenides (TMDs) [31,74,75,158]. The IX binding energies in TMD heterostructures reach hundreds of meV [37,38], making IXs stable at room temperature [49,138]. Propagation of both DXs in TMD monolayers [139–144,159] and IXs in TMD heterostructures [50–58] is intensively studied. However, in spite of long IX lifetimes in TMD heterostructures, orders of magnitude longer than DX lifetimes, a relatively short-range IX propagation with $d_{1/e}$ up ~ 3 μm was reported in the studies of TMD heterostructures.

The short-range of IX propagation originates from in-plane potentials in the TMD heterostructures. In-plane potentials localize excitons and suppress exciton transport. In addition to a long IX lifetime, a long-range IX propagation requires that the in-plane-potential-induced localization and scattering of IXs is weak. In particular, the long-range IX propagation with a high IX diffusion coefficient is realized in GaAs heterostructures with small in-plane disorder potentials [19].

In contrast to GaAs heterostructures, in mechanically stacked TMD heterostructures, the layers are not perfectly aligned and the misalignment can cause significant moiré superlattice

potentials. For $MoSe_2/WSe_2$ heterostructures, similar to the heterostructure studied in this work, the IX energy modulations in moiré potentials are predicted to be in the range of tens of meV [42,44,45,93,94]. Moiré superlattices enable studying excitons in in-plane potentials with the period $b \sim a/\sqrt{\delta\theta^2 + \delta\phi^2}$ typically in the ~ 10 nm range (a is the lattice constant, $\delta\phi$ is the lattice mismatch, $\delta\theta$ is the twist angle deviation from $m\pi/3$, m is an integer) [88,89,91,92,137,160] and the moiré potentials can be affected by atomic reconstruction [46,147–150]. However, for the exciton propagation, the moiré potentials can cause an obstacle and, along with in-plane disorder potentials, can be responsible for limiting the IX propagation distances to $d_{1/e}$ ~ 3 μm in the TMD heterostructures [50–58].

The IX propagation with $d_{1/e}$ ~ 10 μm was realized by applying voltage between the top and bottom electrodes in a TMD heterostructure [161]. The origin of this voltage-controlled IX propagation was discussed in terms of the theoretically predicted [45] tuning of the moiré potential by electric-field, enabling the IX delocalization.

5.2 Results

In this work, we realize in a $MoSe_2/WSe_2$ TMD heterostructure a macroscopically long-range IX propagation with $d_{1/e}$ reaching ~ 100 μm. The strong enhancement of IX propagation is realized using an optical excitation resonant to DXs in the heterostructure. The data show that the strong enhancement of IX propagation is caused by the suppression of IX localization and scattering and is observed in the quantum regime.

The $MoSe_2/WSe_2$ heterostructure is assembled by stacking mechanically exfoliated 2D crystals on a graphite substrate. The $MoSe_2$ and WSe_2 monolayers are encapsulated by dielectric cladding layers of hexagonal boron nitride (hBN). IXs are formed from electrons and holes

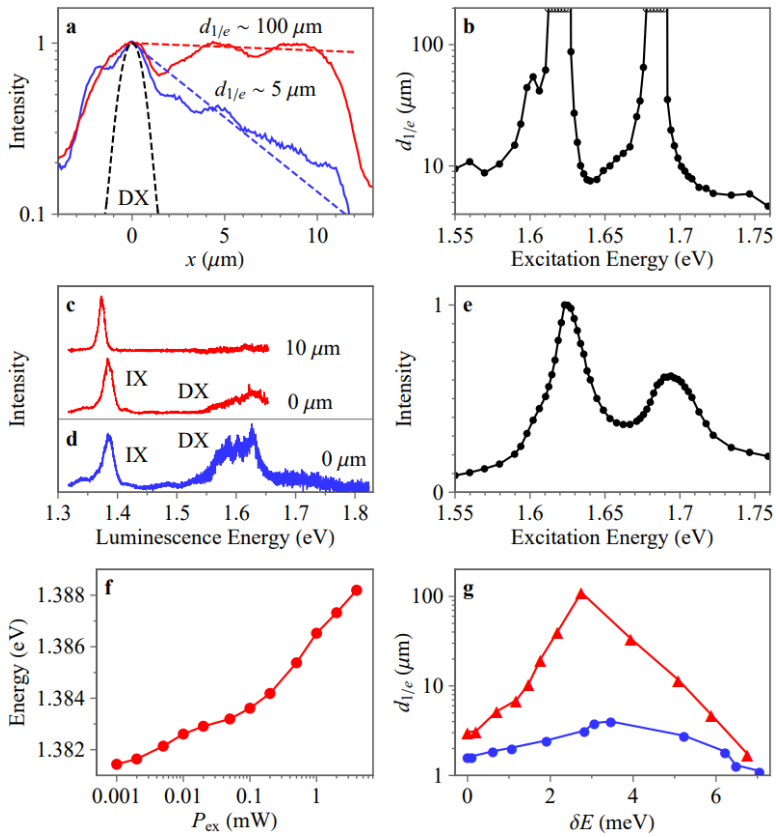

Figure 5.1: Resonant excitation enhances IX propagation. (a) Normalized IX luminescence profiles for laser excitation off ($\boldsymbol{E_{ex}}$ = 1.771 eV, blue) and near $\boldsymbol{E_{ex}}$ = 1.676 eV, red) the DX absorption resonance. The heterostructure active area extends from $\boldsymbol{x}$ = -3 to 12 μm. The blue and red dashed lines show decays with $\boldsymbol{d_{1/e}}$ = 5 and 100 μm, respectively. The black dashed line shows the DX luminescence profile in the WSe_2 monolayer, this profile is close to the laser excitation profile for a short DX propagation. (b) The $\boldsymbol{1/e}$ decay distance of IX luminescence $\boldsymbol{d_{1/e}}$ vs. $\boldsymbol{E_{ex}}$. $\boldsymbol{d_{1/e}}$ are calculated from fitting the IX luminescence profiles to exponential decays in the region $\boldsymbol{x}$ = 0 to 11 μm. The data with the fit indicating $\boldsymbol{d_{1/e}}$ > 100 μm are presented by points on the edge. The finite heterostructure dimensions limit the longest $\boldsymbol{d_{1/e}}$, which can be reliably established, to ~ 100 μm. (c,d) The spectra for resonant [$\boldsymbol{E_{ex}}$ = 1.694 eV, (c)] and non-resonant [$\boldsymbol{E_{ex}}$ = 1.96 eV, (d)] excitation. The relative intensity of the higher-energy DX luminescence is lower for the resonant excitation, evidencing a lower temperature of the exciton system. (e) Integrated IX luminescence intensity vs. $\boldsymbol{E_{ex}}$ showing two absorption peaks corresponding to the $MoSe_2$ and WSe_2 DXs. For data in (a-e), $\boldsymbol{P_{ex}}$ = 0.2 mW, T = 1.7 K. (f) The IX energy at the excitation spot vs. $\boldsymbol{P_{ex}}$. $\boldsymbol{E_{ex}}$ = 1.623 eV, $\boldsymbol{T}$ = 6 K. (g) $\boldsymbol{d_{1/e}}$ vs. the IX energy increase at the excitation spot $\boldsymbol{\delta E}$ for resonant ($\boldsymbol{E_{ex}}$ = 1.623 eV, red) and nonresonant ($\boldsymbol{E_{ex}}$ = 1.96 eV, blue) excitation. $\boldsymbol{T}$ = 6 K. For all data, the ~ 1.5 μm laser spot is centered at $\boldsymbol{x}$ = 0.

confined in adjacent $MoSe_2$ and WSe_2 monolayers, respectively. No voltage is applied in the heterostructure. In the absence of applied voltage, IXs form the ground state in the $MoSe_2/WSe_2$ heterostructure.

The long-range IX propagation with $d_{1/e}$ reaching ~ 100 μm (Figure 5.1a,b) is realized

when the optical excitation has the energy E_{ex} close to the $MoSe_2$ or WSe_2 DX energy (Figure 5.1e). The IX propagation with even longer $d_{1/e}$ is likely realized for E_{ex} close to the DX energy, however, the finite heterostructure dimensions limit the longest $d_{1/e}$, which can be reliably established, to ~ 100 μm (Figure 5.1a,b). In contrast, for a non-resonant excitation, the range of IX propagation is substantially shorter (Figure 5.1a,b). The IX luminescence is traced along the entire IX propagation path from the excitation spot to the edge of the heterostructure (Figure 5.1c). Spatial intensity modulations along the IX propagation will be considered elsewhere.

The factors, which contribute to the enhancement of IX propagation, are outlined below. IXs have built-in electric dipoles ~ ed_{z} (d_{z} is the separation between the electron and hole layers) and the interaction between IXs is repulsive. An enhancement of IX transport with increasing IX density due to the repulsive IX interaction is caused (1) by the suppression of IX localization and scattering and (2) by the IX-interaction-induced drift from the origin.

The data show that the first factor causes the major effect. The nature of the second factor is an increase of IX energy at the excitation spot δE with increasing IX density n (Figure 5.1f) that causes IX drift from the origin [24]. The nearly resonant excitation produces a higher n due to a higher absorption, thus increasing δE and, in turn, the IX drift. However, the higher n and δE can be also achieved for nonresonant excitation using higher excitation powers P_{ex}. Figure 5.1g shows $d_{1/e}$ vs. δE both for the resonant and nonresonant excitation. For the same δE, a much higher $d_{1/e}$ is realized for the resonant excitation. This shows that the effect of IX energy increase at the excitation spot on the enhancement of IX propagation is minor. The strong enhancement of IX propagation at resonant excitation originates from the suppression of localization and scattering of IXs.

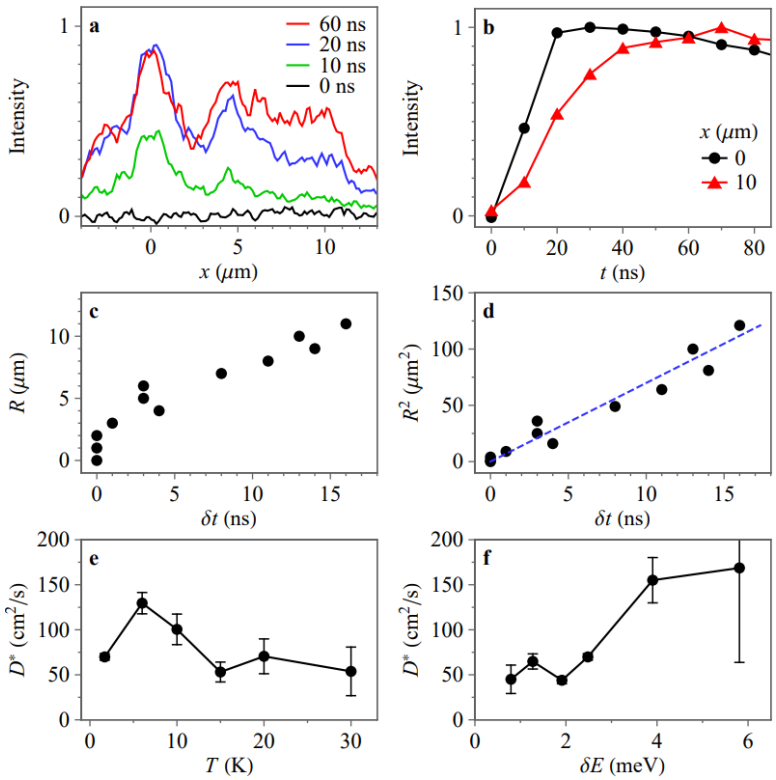

Figure 5.2: IX propagation kinetics. (a) IX luminescence profiles during the laser excitation pulse at different times. (b) Normalized IX luminescence intensity vs. time at different positions. (c) $\boldsymbol{R}$ vs. $\boldsymbol{\delta t}$. $\boldsymbol{\delta t}$ is the time to reach 70% of the maximum intensity at distance $\boldsymbol{R}$ from the excitation spot relative to that time in the excitation spot. (d) $\boldsymbol{R^2}$ vs. $\boldsymbol{\delta t}$. The dashed line is a fit to the data with $\boldsymbol{D^* = R^2/\delta t}$ = 70 cm^2/s. (e,f) $\boldsymbol{D^*}$ vs. temperature (e) and vs. $\boldsymbol{\delta E}$ (f). $\boldsymbol{P_{ex}}$ = 0.15 mW for data in (a-e). $\boldsymbol{T}$ = 1.7 K for data in (a-d,f). For all data, the times are given at the ends of the 10 ns signal integration windows, the excitation pulse starts at $\boldsymbol{t}$ = 0, $\boldsymbol{E_{ex}}$ = 1.694 eV, the ~ 2 μm laser spot is centered at $\boldsymbol{x}$ = 0.

The IX energy increase due to the repulsive interaction δE (Figure 5.1f) can be used for estimating the IX density n. For instance, for the optimal IX propagation conditions, that is for the nearly resonant excitation (Figure 5.1) and the temperature and P_{ex} corresponding to the long $d_{1/e}$ (Figure 5.3), δE ~ 3meV (Figure 5.1f) and an estimate for n using the mean-field "plate capacitor" formula $\delta E = nu_0$ [121] gives $n \sim 2 \times 10^{11}$ cm^{-2} ($u_0 = 4\pi e^2 d_z/\varepsilon$, d_z ~ 0.6 nm, the dielectric constant ε ~ 7.4 [36]). This estimate can be improved by taking into account IX correlations that increases n in comparison to the mean-field estimate. The increase is ~ 3 times for IXs in GaAs heterostructures [18,162]. While similar estimates for correlations in TMD heterostructures are yet unavailable, using the correlation correction similar to that in GaAs gives

the estimated IX density n ~ 6×10^{11} cm^{-2} for the optimal IX propagation conditions. In turn, an estimated temperature of quantum degeneracy $T_{\mathrm{d}} = 2\pi\hbar^2 n/mk_{\mathrm{B}}$ ~ 30 K [38] (m ~ 0.9 m_0 is the IX mass in the TMD heterostructure [163,164]). This estimate shows that the observed strong enhancement of IX propagation at resonant excitation due to the suppression of IX localization and scattering occurs (i) in the quantum regime and (ii) in a dilute IX gas with the densities below the Mott transition density n_{Mott} > 10^{12} cm^{-2} [38,165].

In the quantum regime, the pioneering works on IXs predict IX superfluidity [9] that suppresses the IX localization and scattering. However, a theory of quantum transport of IXs in TMD heterostructures, in particular in the presence of moiré potentials, yet need to be developed. Therefore, below, we use the classical drift-diffusion model [24] (section 5.3), to discuss the characteristics of IX propagation.

For instance, within the drift-diffusion model of IX transport [24], the suppression of IX localization and scattering is accounted for by screening of the in-plane potential by repulsively interacting IXs. The screening of in-plane potential is more effective when the excitation is close to the DX resonances. In particular, heating of the exciton system by the nearly resonant excitation is, in general, smaller than for non-resonant excitation, and the colder IXs can screen the in-plane potential more effectively [18,24]. The most efficient screening of the in-plane potential by IXs is realized below the temperature of IX condensation [166].

Figure 5.2 shows the kinetics of IX propagation from the excitation spot for the nearly optimal propagation conditions. The IX kinetics is measured during the rectangular-shaped laser excitation pulses with the duration 100 ns and period 300 ns. The 200 ns off time exceeds the IX lifetime (Figure 5.4) and is sufficient for a substantial decay of the IX signal. The IX luminescence at locations away from the excitation spot is delayed in comparison to the IX

luminescence in the excitation spot (Figure 5.2a,b). The delay times δt for the IX cloud to expand to the locations separated by distance R from the origin allow estimating the IX transport characteristics. Fitting R vs. δt by $R^2 \sim D^* \delta t$ (Figure 5.2d), gives an estimate for the effective IX diffusion coefficient D^* ~ 70 cm^2/s.

For a diffusive IX propagation, both IX drift and diffusion contribute to the expansion of IX cloud. With increasing distance from the origin, both the IX density n and IX interaction energy $\delta E \sim n u_0$ decrease. The IX energy gradient causes the IX drift away from the origin. Fitting an IX cloud expansion by $R^2 \sim D^* \delta t$ probes the effective IX diffusion coefficient $D^* = D + \mu n u_0$, which includes both the diffusion and drift due to the density gradient [167]. The IX mobility μ can be estimated using the Einstein relation $\mu = D/k_B T$, giving $D^* = D(1 + n u_0/k_B T)$. For $n u_0$ ~ 3 meV at P_{ex} = 0.15 mW (Figure 5.1f), D^* ~ 70 cm^2/s (Figure 5.2d), and T = 1.7 K, this equation gives an estimate for the IX diffusion coefficient D ~ 4 cm^2/s. In turn, the estimated IX mobility $\mu = D/k_B T$ ~ 3×10^4 cm^2/(eV s).

The data R vs. δt (Figure 5.2c) indicate that an IX cloud expansion occurs with a nearly constant velocity after first few ns. The estimated average velocity of the IX cloud expansion for the time range δt = 1 – 20 ns, $v = \delta R/\delta t$ ~ 5×10^4 cm/s (Figure 5.2c).

The variation of D^* with temperature and δE is presented in Figure 5.2e,f (δE characterizes the IX density n at the origin). An enhancement of D^* with density can be in principle explained by the classical IX drift and diffusion: both the exciton diffusion coefficient D and the IX drift should increase with n, the former due to the enhanced screening of in-plane potential and the latter due to the enhanced δE at the origin [24], for details see section 5.3. An enhancement of IX propagation with density due to these factors was observed in earlier studies of both GaAs and TMD heterostructures, see e.g. Refs. [18,24,51,57,58]. As outlined above, the

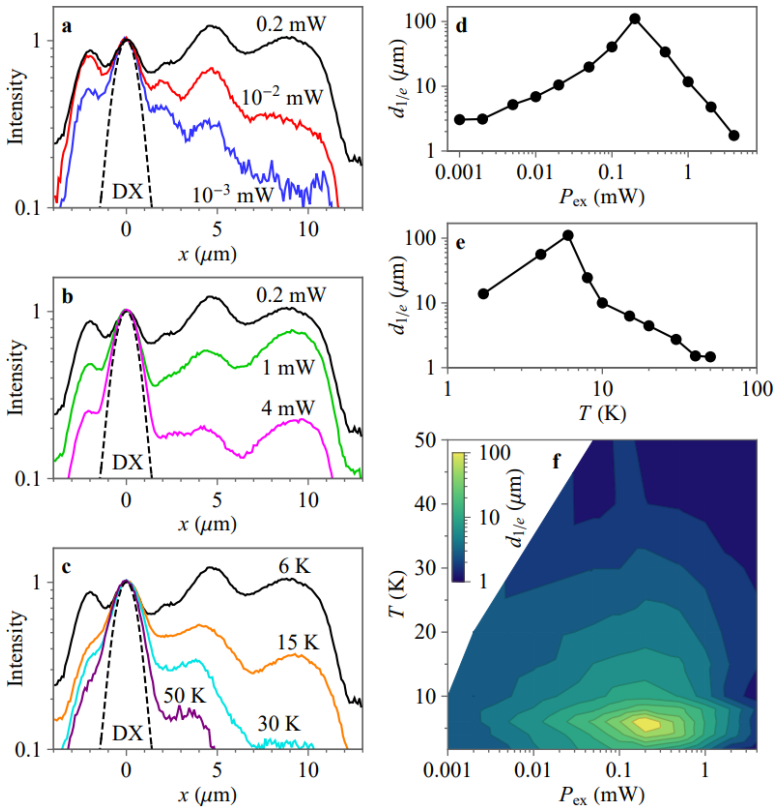

Figure 5.3: $P-T$ diagram for IX propagation length. (a-c) Normalized IX luminescence profiles for different $\boldsymbol{P_{ex}}$ (a,b) and temperatures (c). The dashed line shows the DX luminescence profile in the WSe_2 monolayer, this profile is close to the laser excitation profile for a short DX propagation. $\boldsymbol{T}$ = 6 K (a,b,d), $\boldsymbol{P_{ex}}$ = 0.2 mW (c,e). (d,e) The $\boldsymbol{1/e}$ decay distance of IX luminescence $\boldsymbol{d_{1/e}}$ vs. $\boldsymbol{P_{ex}}$ (d) and vs. temperature (e). (f) Contour plot showing the decay distance $\boldsymbol{d_{1/e}}$ vs. both $\boldsymbol{P_{ex}}$ and temperature. The greatest IX propagation occurs at $\boldsymbol{T}$ ~ 6 K and $\boldsymbol{P_{ex}}$ ~ 0.2 mW. For all data, $\boldsymbol{E_{ex}}$ = 1.623 eV, the ~ 1.5 μm laser spot is centered at $\boldsymbol{x}$ = 0.

long-range IX propagation at resonant excitation, presented here, originates from the suppression of IX localization and scattering in the quantum dilute IX gas and is qualitatively different from the IX propagation in earlier studies of TMD heterostructures.

A reduction of D^* with temperature is observed for T > 6 K (Figure 5.2e). A suppression of IX propagation with temperature is consistent with the expected behavior for quantum exciton transport [9] and complies with the reduction of superfluid density with temperature: A nearly linear reduction of the superfluid density with temperature at temperatures below the Berezinskii-Kosterlitz-Thouless transition is found in the theory [168]. We note however that more accurate measurements are needed for a quantitative comparison with the theory. This

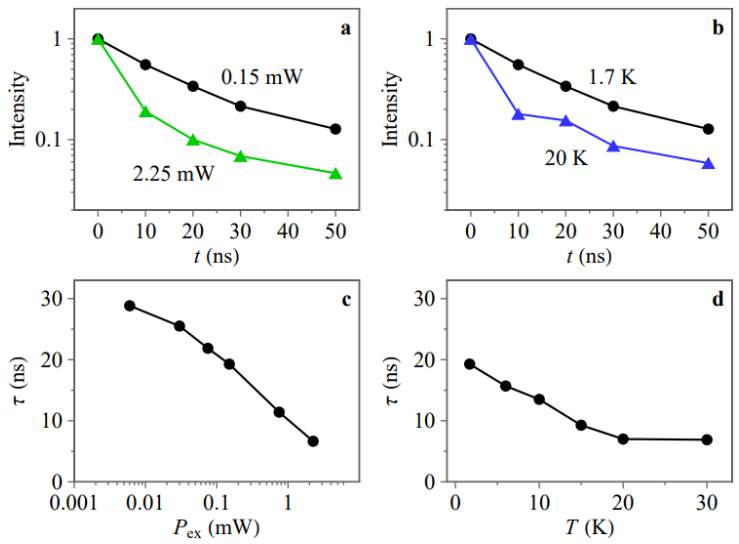

Figure 5.4: IX decay kinetics. (a,b) Spatially integrated IX luminescence intensity vs. time for different $\boldsymbol{P_{ex}}$ (a) and temperatures (b). The times are given at the ends of the 10 ns signal integration windows. The excitation pulse ends at $\boldsymbol{t}$ = 0. (c,d) The IX lifetime $\boldsymbol{\tau}$ vs. $\boldsymbol{P_{ex}}$ (c) and vs. temperature (d). $\boldsymbol{\tau}$ is the initial decay time after the excitation pulse end. $\boldsymbol{T}$ = 1.7 K (a,c), $\boldsymbol{P_{ex}}$ = 0.15 mW (b,d). For all data, $\boldsymbol{E_{ex}}$ = 1.694 eV.

forms a subject for future works. In particular, an increase of D^* with temperature at T < 6 K (Figure 5.2e) need to be understood. In general, the contributions of both the normal and superfluid components to the quantum exciton transport should be explored. The classical drift-diffusion model [24] is inconsistent with the observed temperature dependence of IX transport, see section 5.3.

The excitation power and temperature dependence of IX propagation is presented in Figure 5.3. With increasing P_{ex}, the IX propagation distance $d_{1/e}$ changes nonmonotonically. A relatively short-range IX propagation is observed at the lowest P_{ex} (Figure 5.3a,d). This is consistent with the IX localization in the in-plane potential. Increasing P_{ex} and, in turn, IX density n suppresses the IX localization and scattering and results in an enhancement of IX propagation. The longest IX propagation is achieved at P_{ex} ~ 0.2 mW and the further enhancement of P_{ex} leads to the suppression of IX propagation (Figure 5.3b,d). This suppression is related to the reduction of IX lifetime at high P_{ex} (Figure 5.4c).

With increasing temperature, the IX propagation first enhances, reaches maximum around T ~ 6 K, and reduces at higher temperatures (Figure 5.3e). This behavior is related to the temperature dependence of D^* (Figure 5.2e), with the suppression at high temperatures further enhanced by the reduction of IX lifetime (Figure 5.4d). The measured $P_{\mathrm{ex}} - T$ diagram for the IX propagation distance $d_{1/e}$ is shown in Figure 5.3f.

Figure 5.4 shows the IX luminescence decay kinetics after the laser excitation pulse is off. The IX decay times τ (Figure 5.4) are orders of magnitude longer than the DX decay times [151]. Both increasing P_{ex} (Figure 5.4a,c) and temperature (Figure 5.4b,d) lead to a reduction of τ. This reduction of τ contributes to suppressing the IX propagation at high excitation powers and temperatures as outlined above.

5.3 Drift-Diffusion Model of IX Transport

The drift-diffusion model of IX transport [24,169,170], used for the estimates for IX diffusion coefficient and mobility in the main text, is outlined in this section. Within this model, IX transport is described by the equation for IX density n

$$\frac{\partial n}{\partial t} = \nabla[D\nabla n + \mu\nabla(nu_0)] + \Lambda - \frac{n}{\tau} \tag{5.1}$$

The first and second terms in square brackets in Equation 5.1 describe IX diffusion and drift currents, respectively. The latter originates from the IX repulsive dipolar interactions and is approximated by the mean-field "plate capacitor" formula for the IX energy shift with density $\delta E = nu_0$, $u_0 = 4\pi e^2 d_{\mathrm{z}}/\varepsilon$ [121]. The diffusion coefficient

$$D = D^{(0)} exp\left[-U^{(0)}/(k_{\mathrm{B}}T + nu_0)\right] \tag{5.2}$$

accounts for the temperature- and density-dependent screening of the long-range-correlated in-plane potential landscape by interacting IXs, $D^{(0)}$ is the diffusion coefficient in the absence of in-

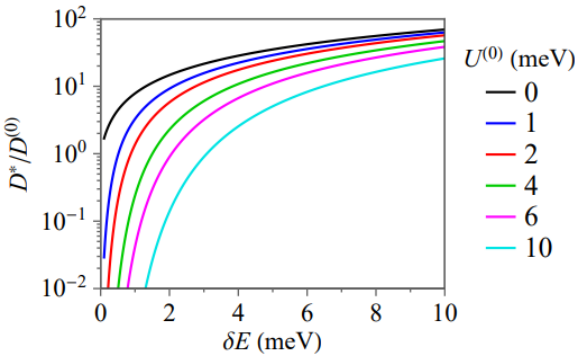

Figure 5.5: Dependence of D^* on IX interaction energy. $D^*/D^{(0)}$ vs. δE for different $U^{(0)}$. T = 1.7 K.

plane potential and $U^{(0)}/2$ is the amplitude of the in-plane potential [24,169,170]. The IX mobility μ is given by the Einstein relation $\mu = D/k_B T$. The IX generation rate Λ has a profile of the laser excitation spot. τ is the IX lifetime.

Both the IX-interaction-induced screening of in-plane potential and the IX-interaction-induced drift from the origin contribute to the enhancement of IX transport with increasing IX density n. In particular, within the classical drift-diffusion model [24,169,170], the enhancement of IX transport due to the IX-interaction-induced screening of in-plane potential is described by Equation 5.2, while the enhancement of IX transport due to the IX-interaction-induced drift from the origin is described by Equation 5.3

$$D^* = D(1 + nu_0/k_B T) \tag{5.3}$$

Equations 5.2 and 5.3 show that within the classical drift-diffusion model [24,169,170], both D and D^* should increase with density for any $U^{(0)}$ (Figure 5.5). The variation of D^* increases with $U^{(0)}$ (Figure 5.6), and the variation of D^* in the experiment (~ 3 times for δE = 1 – 4 meV, Figure 5.2f) corresponds to vanishing in-plane potential ($U^{(0)}$ < 1 meV). The predicted $U^{(0)}$ for $MoSe_2/WSe_2$ heterobilayers with R and H stacking is ~100 and ~ 25 meV, respectively [44,45].

Equations 5.2 and 5.33 show that within the classical drift-diffusion model [24,169,170],

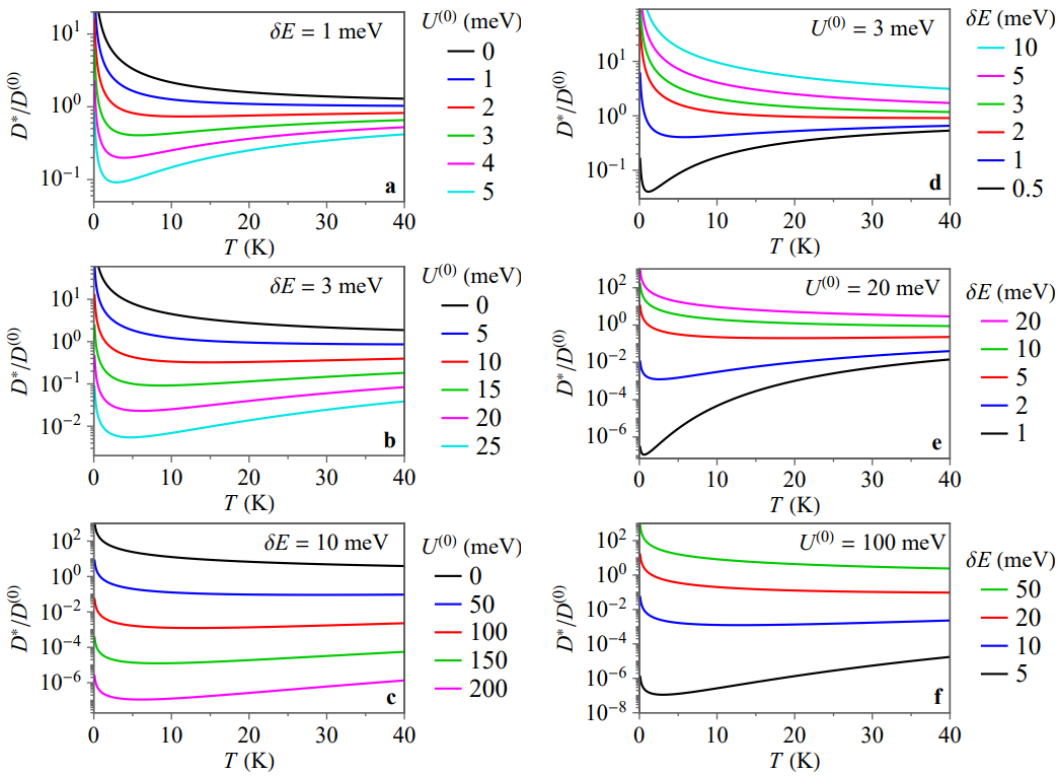

Figure 5.6: Dependence of D^* on temperature. $D^*/D^{(0)}$ vs. T for different δE and $U^{(0)}$.

D should increase with temperature for any $U^{(0)}$, however, the dependence of D^* on temperature is nonmonotonic (Figure 5.6). Within this model, D^* increases with temperature when $U^{(0)} > \delta E(1 + \delta E/k_B T)$. The classical drift-diffusion model [24,169,170] (Equations 5.1–3, Figure 5.6) is inconsistent with the observed temperature dependence of IX transport (Figure 5.2e): If D^* increases with temperature at $T \sim 2 – 6$ K, as in the experiment, then within the model D^* should also increase with temperature at higher temperatures [if $U^{(0)} > \delta E(1 + \delta E/k_B T)$ at lower T, this inequality holds for higher T, see e.g. the black lines in Figure 5.6d,e,f] that is inconsistent with the experiment; If D^* reduces with temperature at $T > 6$ K, as in the experiment, then within the model D^* should also reduce with temperature at lower temperatures [if $U^{(0)} < \delta E(1 + \delta E/k_B T)$ at higher T, this inequality holds for lower T, see e.g. the black lines in Figure 5.6a,b,c)] that is inconsistent with the experiment.

5.4 Conclusions and Outlook

In summary, a macroscopically long-range IX propagation with the decay distances $d_{1/e}$ reaching ~ 100 μm is observed in a van der Waals $MoSe_2/WSe_2$ heterostructure. The strong enhancement of IX propagation is realized using an optical excitation resonant to DXs in the heterostructure. The strong enhancement of IX propagation originates from the suppression of IX localization and scattering and is observed in the quantum regime.

The observation of long-range IX transport in the presence of predicted strong localization potentials suggests a path forward for the development of excitonic devices in the TMD system. It is the subject for future work to identify the precise causes of the strong suppression of IX scattering and localization potentials.

5.5 Acknowledgements

The text of chapter 5, in part, has been submitted for publication of the material, L. H. Fowler-Gerace, Z. Zhou, E. A. Szwed, and L. V. Butov, Long-range quantum transport of indirect excitons in van der Waals heterostructure, https://arxiv.org/abs/2204.09760 (2022), where the dissertation author is the first author. The co-authors in these publications directed, supervised, and co-worked on the research which forms the basis of this chapter.

Bibliography

[1] Gordon E Moore, *Cramming More Components onto Integrated Circuits*, Electronics **38**, 114 (1965).

[2] C. E. Leiserson, N. C. Thompson, J. S. Emer, B. C. Kuszmaul, B. W. Lampson, D. Sanchez, and T. B. Schardl, *There's Plenty of Room at the Top: What Will Drive Computer Performance after Moore's Law?*, Science **368**, eaam9744 (2020).

[3] L. V. Butov, *Excitonic Devices*, Superlattices and Microstructures **108**, 2 (2017).

[4] M. Baldo and V. Stojanović, *Excitonic Interconnects*, Nature Photon **3**, 10 (2009).

[5] A. A. High, A. T. Hammack, L. V. Butov, M. Hanson, and A. C. Gossard, *Exciton Optoelectronic Transistor*, Opt. Lett., OL **32**, 2466 (2007).

[6] A. Vinattieri, J. Shah, T. C. Damen, D. S. Kim, L. N. Pfeiffer, M. Z. Maialle, and L. J. Sham, *Exciton Dynamics in GaAs Quantum Wells under Resonant Excitation*, Phys. Rev. B **50**, 10868 (1994).

[7] S. Charbonneau, M. L. W. Thewalt, E. S. Koteles, and B. Elman, *Transformation of Spatially Direct to Spatially Indirect Excitons in Coupled Double Quantum Wells*, Phys. Rev. B **38**, 6287 (1988).

[8] J. E. Golub, K. Kash, J. P. Harbison, and L. T. Florez, *Long-Lived Spatially Indirect Excitons in Coupled GaAs/Al_xGa_{1-x}As Quantum Wells*, Phys. Rev. B **41**, 8564 (1990).

[9] Y. E. Lozovik and V. I. Yudson, *New Mechanism for Superconductivity: Pairing between Spatially Separated Electrons and Holes*, Sov. Phys. - JETP (Engl. Transl.); (United States) **71**, 738 (1976).

[10] L. V. Butov, A. Zrenner, G. Abstreiter, G. Böhm, and G. Weimann, *Condensation of Indirect Excitons in Coupled AlAs/GaAs Quantum Wells*, Phys. Rev. Lett. **73**, 304 (1994).

[11] L. V. Butov and A. I. Filin, *Anomalous Transport and Luminescence of Indirect Excitons in AlAs/GaAs Coupled Quantum Wells as Evidence for Exciton Condensation*, Phys. Rev. B **58**, 1980 (1998).

[12] L. V. Butov, A. L. Ivanov, A. Imamoglu, P. B. Littlewood, A. A. Shashkin, V. T. Dolgopolov, K. L. Campman, and A. C. Gossard, *Stimulated Scattering of Indirect Excitons in Coupled Quantum Wells: Signature of a Degenerate Bose-Gas of Excitons*, Phys. Rev. Lett. **86**, 5608 (2001).

[13] L. V. Butov, A. C. Gossard, and D. S. Chemla, *Macroscopically Ordered State in an Exciton System*, Nature **418**, 6899 (2002).

[14] A. A. High, J. R. Leonard, A. T. Hammack, M. M. Fogler, L. V. Butov, A. V. Kavokin, K. L. Campman, and A. C. Gossard, *Spontaneous Coherence in a Cold Exciton Gas*, Nature **483**, 7391 (2012).

[15] J. R. Leonard, L. Hu, A. A. High, A. T. Hammack, C. Wu, L. V. Butov, K. L. Campman, and A. C. Gossard, *Moiré Pattern of Interference Dislocations in Condensate of Indirect Excitons*, Nat Commun **12**, 1 (2021).

[16] L. V. Butov and A. I. Filin, *Energy Relaxation and Transport of Indirect Excitons in AlAs/GaAs Coupled Quantum Wells in Magnetic Field*, J. Exp. Theor. Phys. **87**, 608 (1998).

[17] A. A. High, A. T. Hammack, L. V. Butov, L. Mouchliadis, A. L. Ivanov, M. Hanson, and A. C. Gossard, *Indirect Excitons in Elevated Traps*, Nano Lett. **9**, 2094 (2009).

[18] M. Remeika, J. C. Graves, A. T. Hammack, A. D. Meyertholen, M. M. Fogler, L. V. Butov, M. Hanson, and A. C. Gossard, *Localization-Delocalization Transition of Indirect Excitons in Lateral Electrostatic Lattices*, Phys. Rev. Lett. **102**, 186803 (2009).

[19] C. J. Dorow, M. W. Hasling, D. J. Choksy, J. R. Leonard, L. V. Butov, K. W. West, and L. N. Pfeiffer, *High-Mobility Indirect Excitons in Wide Single Quantum Well*, Appl. Phys. Lett. **113**, 212102 (2018).

[20] M. Hagn, A. Zrenner, G. Böhm, and G. Weimann, *Electric-field-induced Exciton Transport in Coupled Quantum Well Structures*, Appl. Phys. Lett. **67**, 232 (1995).

[21] J. R. Leonard, M. Remeika, M. K. Chu, Y. Y. Kuznetsova, A. A. High, L. V. Butov, J. Wilkes, M. Hanson, and A. C. Gossard, *Transport of Indirect Excitons in a Potential Energy Gradient*, Appl. Phys. Lett. **100**, 231106 (2012).

[22] A. G. Winbow, J. R. Leonard, M. Remeika, Y. Y. Kuznetsova, A. A. High, A. T. Hammack, L. V. Butov, J. Wilkes, A. A. Guenther, A. L. Ivanov, M. Hanson, and A. C. Gossard, *Electrostatic Conveyer for Excitons*, Phys. Rev. Lett. **106**, 196806 (2011).

[23] A. T. Hammack, N. A. Gippius, S. Yang, G. O. Andreev, L. V. Butov, M. Hanson, and A. C. Gossard, *Excitons in Electrostatic Traps*, Journal of Applied Physics **99**, 066104 (2006).

[24] A. L. Ivanov, L. E. Smallwood, A. T. Hammack, S. Yang, L. V. Butov, and A. C. Gossard, *Origin of the Inner Ring in Photoluminescence Patterns of Quantum Well Excitons*, EPL **73**, 920 (2006).

[25] A. A. High, E. E. Novitskaya, L. V. Butov, M. Hanson, and A. C. Gossard, *Control of Exciton Fluxes in an Excitonic Integrated Circuit*, Science **321**, 229 (2008).

[26] D. Chemla, D. Miller, P. Smith, A. Gossard, and W. Wiegmann, *Room Temperature Excitonic Nonlinear Absorption and Refraction in GaAs/AlGaAs Multiple Quantum Well Structures*, IEEE Journal of Quantum Electronics **20**, 265 (1984).

[27] K. Sivalertporn, L. Mouchliadis, A. L. Ivanov, R. Philp, and E. A. Muljarov, *Direct and Indirect Excitons in Semiconductor Coupled Quantum Wells in an Applied Electric Field*, Phys. Rev. B **85**, 045207 (2012).

[28] A. Zrenner, P. Leeb, J. Schäfer, G. Böhm, G. Weimann, J. M. Worlock, L. T. Florez, and J. P. Harbison, *Indirect Excitons in Coupled Quantum Well Structures*, Surface Science **263**, 496 (1992).

[29] C. Morhain, T. Bretagnon, P. Lefebvre, X. Tang, P. Valvin, T. Guillet, B. Gil, T. Taliercio, M. Teisseire-Doninelli, B. Vinter, and C. Deparis, *Internal Electric Field in Wurtzite ZnO/$Zn_{0.78}Mg_{0.22}$ Quantum Wells*, Phys. Rev. B **72**, 241305 (2005).

[30] G. Fiori, F. Bonaccorso, G. Iannaccone, T. Palacios, D. Neumaier, A. Seabaugh, S. K. Banerjee, and L. Colombo, *Electronics Based on Two-Dimensional Materials*, Nature Nanotech **9**, 10 (2014).

[31] A. K. Geim and I. V. Grigorieva, *Van Der Waals Heterostructures*, Nature **499**, 7459 (2013).

[32] B. Radisavljevic, A. Radenovic, J. Brivio, V. Giacometti, and A. Kis, *Single-Layer MoS_2 Transistors*, Nature Nanotech **6**, 3 (2011).

[33] K. F. Mak, C. Lee, J. Hone, J. Shan, and T. F. Heinz, *Atomically Thin MoS_2: A New Direct-Gap Semiconductor*, Phys. Rev. Lett. **105**, 136805 (2010).

[34] J. K. Ellis, M. J. Lucero, and G. E. Scuseria, *The Indirect to Direct Band Gap Transition in Multilayered MoS_2 as Predicted by Screened Hybrid Density Functional Theory*, Appl. Phys. Lett. **99**, 261908 (2011).

[35] I. Strzalkowski, S. Joshi, and C. R. Crowell, *Dielectric Constant and Its Temperature Dependence for GaAs, CdTe, and ZnSe*, Appl. Phys. Lett. **28**, 350 (1976).

[36] A. Laturia, M. L. Van de Put, and W. G. Vandenberghe, *Dielectric Properties of Hexagonal Boron Nitride and Transition Metal Dichalcogenides: From Monolayer to Bulk*, Npj 2D Mater Appl **2**, 1 (2018).

[37] T. Deilmann and K. S. Thygesen, *Interlayer Trions in the MoS_2/WS_2 van Der Waals Heterostructure*, Nano Lett. **18**, 1460 (2018).

[38] M. M. Fogler, L. V. Butov, and K. S. Novoselov, *High-Temperature Superfluidity with Indirect Excitons in van Der Waals Heterostructures*, Nat Commun **5**, 1 (2014).

[39] F. Wu, F. Qu, and A. H. MacDonald, *Exciton Band Structure of Monolayer MoS_2*, Phys. Rev. B **91**, 075310 (2015).

[40] H. Yu, Y. Wang, Q. Tong, X. Xu, and W. Yao, *Anomalous Light Cones and Valley Optical Selection Rules of Interlayer Excitons in Twisted Heterobilayers*, Phys. Rev. Lett. **115**, 187002 (2015).

[41] P. K. Nayak, Y. Horbatenko, S. Ahn, G. Kim, J.-U. Lee, K. Y. Ma, A.-R. Jang, H. Lim, D. Kim, S. Ryu, H. Cheong, N. Park, and H. S. Shin, *Probing Evolution of Twist-Angle-Dependent Interlayer Excitons in $MoSe_2/WSe_2$ van Der Waals Heterostructures*, ACS Nano **11**, 4041 (2017).

[42] C. Zhang, C.-P. Chuu, X. Ren, M.-Y. Li, L.-J. Li, C. Jin, M.-Y. Chou, and C.-K. Shih, *Interlayer Couplings, Moiré Patterns, and 2D Electronic Superlattices in MoS_2/WSe_2 Hetero-Bilayers*, Science Advances **3**, e1601459 (2017).

[43] P.-Y. Chen, X.-Q. Zhang, Y.-Y. Lai, E.-C. Lin, C.-A. Chen, S.-Y. Guan, J.-J. Chen, Z.-H. Yang, Y.-W. Tseng, S. Gwo, C.-S. Chang, L.-J. Chen, and Y.-H. Lee, *Tunable Moiré Superlattice of Artificially Twisted Monolayers*, Advanced Materials **31**, 1901077 (2019).

[44] F. Wu, T. Lovorn, and A. H. MacDonald, *Theory of Optical Absorption by Interlayer Excitons in Transition Metal Dichalcogenide Heterobilayers*, Phys. Rev. B **97**, 035306 (2018).

[45] H. Yu, G.-B. Liu, J. Tang, X. Xu, and W. Yao, *Moiré Excitons: From Programmable Quantum Emitter Arrays to Spin-Orbit–Coupled Artificial Lattices*, Science Advances **3**, e1701696 (2017).

[46] M. R. Rosenberger, H.-J. Chuang, M. Phillips, V. P. Oleshko, K. M. McCreary, S. V. Sivaram, C. S. Hellberg, and B. T. Jonker, *Twist Angle-Dependent Atomic Reconstruction and Moiré Patterns in Transition Metal Dichalcogenide Heterostructures*, ACS Nano **14**, 4550 (2020).

[47] P. Rivera, J. R. Schaibley, A. M. Jones, J. S. Ross, S. Wu, G. Aivazian, P. Klement, K. Seyler, G. Clark, N. J. Ghimire, J. Yan, D. G. Mandrus, W. Yao, and X. Xu, *Observation of Long-Lived Interlayer Excitons in Monolayer $MoSe_2$–WSe_2 Heterostructures*, Nat Commun **6**, 1 (2015).

[48] P. Nagler, G. Plechinger, M. V. Ballottin, A. Mitioglu, S. Meier, N. Paradiso, C. Strunk, A. Chernikov, P. C. M. Christianen, C. Schüller, and T. Korn, *Interlayer Exciton Dynamics in a Dichalcogenide Monolayer Heterostructure*, 2D Mater. **4**, 025112 (2017).

[49] E. V. Calman, M. M. Fogler, L. V. Butov, S. Hu, A. Mishchenko, and A. K. Geim, *Indirect Excitons in van Der Waals Heterostructures at Room Temperature*, Nat Commun **9**, 1 (2018).

[50] P. Rivera, K. L. Seyler, H. Yu, J. R. Schaibley, J. Yan, D. G. Mandrus, W. Yao, and X. Xu, *Valley-Polarized Exciton Dynamics in a 2D Semiconductor Heterostructure*, Science **351**, 688 (2016).

[51] L. A. Jauregui, A. Y. Joe, K. Pistunova, D. S. Wild, A. A. High, Y. Zhou, G. Scuri, K. De Greve, A. Sushko, C.-H. Yu, T. Taniguchi, K. Watanabe, D. J. Needleman, M. D. Lukin, H. Park, and P. Kim, *Electrical Control of Interlayer Exciton Dynamics in Atomically Thin Heterostructures*, Science **366**, 870 (2019).

[52] D. Unuchek, A. Ciarrocchi, A. Avsar, K. Watanabe, T. Taniguchi, and A. Kis, *Room-Temperature Electrical Control of Exciton Flux in a van Der Waals Heterostructure*, Nature **560**, 7718 (2018).

[53] D. Unuchek, A. Ciarrocchi, A. Avsar, Z. Sun, K. Watanabe, T. Taniguchi, and A. Kis, *Valley-Polarized Exciton Currents in a van Der Waals Heterostructure*, Nat. Nanotechnol. **14**, 12 (2019).

[54] Y. Liu, K. Dini, Q. Tan, T. Liew, K. S. Novoselov, and W. Gao, *Electrically Controllable Router of Interlayer Excitons*, Science Advances **6**, eaba1830 (2020).

[55] Z. Huang, Y. Liu, K. Dini, Q. Tan, Z. Liu, H. Fang, J. Liu, T. Liew, and W. Gao, *Robust Room Temperature Valley Hall Effect of Interlayer Excitons*, Nano Lett. **20**, 1345 (2020).

[56] L. Yuan, B. Zheng, J. Kunstmann, T. Brumme, A. B. Kuc, C. Ma, S. Deng, D. Blach, A. Pan, and L. Huang, *Twist-Angle-Dependent Interlayer Exciton Diffusion in WS_2–WSe_2 Heterobilayers*, Nat. Mater. **19**, 6 (2020).

[57] J. Wang, Q. Shi, E.-M. Shih, L. Zhou, W. Wu, Y. Bai, D. Rhodes, K. Barmak, J. Hone, C. R. Dean, and X.-Y. Zhu, *Diffusivity Reveals Three Distinct Phases of Interlayer Excitons in $MoSe_2$/WSe_2 Heterobilayers*, Phys. Rev. Lett. **126**, 106804 (2021).

[58] Z. Sun, A. Ciarrocchi, F. Tagarelli, J. F. Gonzalez Marin, K. Watanabe, T. Taniguchi, and A. Kis, *Excitonic Transport Driven by Repulsive Dipolar Interaction in a van Der Waals Heterostructure*, Nat. Photon. **16**, 1 (2022).

[59] J. Choi, W.-T. Hsu, L.-S. Lu, L. Sun, H.-Y. Cheng, M.-H. Lee, J. Quan, K. Tran, C.-Y. Wang, M. Staab, K. Jones, T. Taniguchi, K. Watanabe, M.-W. Chu, S. Gwo, S. Kim, C.-K. Shih, X. Li, and W.-H. Chang, *Moiré Potential Impedes Interlayer Exciton Diffusion in van Der Waals Heterostructures*, Science Advances **6**, eaba8866 (2020).

[60] L. H. Brixner, *Preparation and Properties of the Single Crystalline AB2-Type Selenides and Tellurides of Niobium, Tantalum, Molybdenum and Tungsten*, Journal of Inorganic and Nuclear Chemistry **24**, 257 (1962).

[61] S. Shree, A. George, T. Lehnert, C. Neumann, M. Benelajla, C. Robert, X. Marie, K. Watanabe, T. Taniguchi, U. Kaiser, B. Urbaszek, and A. Turchanin, *High Optical Quality of MoS_2 Monolayers Grown by Chemical Vapor Deposition*, 2D Mater. **7**, 015011 (2019).

[62] F. Withers, O. Del Pozo-Zamudio, A. Mishchenko, A. P. Rooney, A. Gholinia, K. Watanabe, T. Taniguchi, S. J. Haigh, A. K. Geim, A. I. Tartakovskii, and K. S. Novoselov, *Light-Emitting Diodes by Band-Structure Engineering in van Der Waals Heterostructures*, Nature Mater **14**, 3 (2015).

[63] H. Li, G. Lu, Z. Yin, Q. He, H. Li, Q. Zhang, and H. Zhang, *Optical Identification of Single- and Few-Layer MoS_2 Sheets*, Small **8**, 682 (2012).

[64] M. Alloing, M. Beian, M. Lewenstein, D. Fuster, Y. González, L. González, R. Combescot, M. Combescot, and F. Dubin, *Evidence for a Bose-Einstein Condensate of Excitons*, EPL **107**, 10012 (2014).

[65] S. Yang, L. V. Butov, B. D. Simons, K. L. Campman, and A. C. Gossard, *Fluctuation and Commensurability Effect of Exciton Density Wave*, Phys. Rev. B **91**, 245302 (2015).

[66] A. A. High, A. T. Hammack, J. R. Leonard, S. Yang, L. V. Butov, T. Ostatnický, M. Vladimirova, A. V. Kavokin, T. C. H. Liew, K. L. Campman, and A. C. Gossard, *Spin Currents in a Coherent Exciton Gas*, Phys. Rev. Lett. **110**, 246403 (2013).

[67] J. R. Leonard, A. A. High, A. T. Hammack, M. M. Fogler, L. V. Butov, K. L. Campman, and A. C. Gossard, *Pancharatnam–Berry Phase in Condensate of Indirect Excitons*, Nat Commun **9**, 1 (2018).

[68] A. Gärtner, A. W. Holleitner, J. P. Kotthaus, and D. Schuh, *Drift Mobility of Long-Living Excitons in Coupled GaAs Quantum Wells*, Appl. Phys. Lett. **89**, 052108 (2006).

[69] S. Lazić, A. Violante, K. Cohen, R. Hey, R. Rapaport, and P. V. Santos, *Scalable Interconnections for Remote Indirect Exciton Systems Based on Acoustic Transport*, Phys. Rev. B **89**, 085313 (2014).

[70] G. Grosso, J. Graves, A. T. Hammack, A. A. High, L. V. Butov, M. Hanson, and A. C. Gossard, *Excitonic Switches Operating at around 100 K*, Nature Photon **3**, 10 (2009).

[71] P. Lefebvre, S. Kalliakos, T. Bretagnon, P. Valvin, T. Taliercio, B. Gil, N. Grandjean, and J. Massies, *Observation and Modeling of the Time-Dependent Descreening of Internal Electric Field in a Wurtzite $GaN/Al_{0.15}Ga_{0.85}N$ Quantum Well after High Photoexcitation*, Phys. Rev. B **69**, 035307 (2004).

[72] F. Fedichkin, T. Guillet, P. Valvin, B. Jouault, C. Brimont, T. Bretagnon, L. Lahourcade, N. Grandjean, P. Lefebvre, and M. Vladimirova, *Room-Temperature Transport of Indirect Excitons in (Al, Ga)N/ GaN Quantum Wells*, Phys. Rev. Applied **6**, 014011 (2016).

[73] F. Chiaruttini, T. Guillet, C. Brimont, B. Jouault, P. Lefebvre, J. Vives, S. Chenot, Y. Cordier, B. Damilano, and M. Vladimirova, *Trapping Dipolar Exciton Fluids in GaN/(AlGa)N Nanostructures*, Nano Lett. **19**, 4911 (2019).

[74] Z. Ye, T. Cao, K. O'Brien, H. Zhu, X. Yin, Y. Wang, S. G. Louie, and X. Zhang, *Probing Excitonic Dark States in Single-Layer Tungsten Disulphide*, Nature **513**, 7517 (2014).

[75] A. Chernikov, T. C. Berkelbach, H. M. Hill, A. Rigosi, Y. Li, O. B. Aslan, D. R. Reichman, M. S. Hybertsen, and T. F. Heinz, *Exciton Binding Energy and Nonhydrogenic Rydberg Series in Monolayer WS_2*, Phys. Rev. Lett. **113**, 076802 (2014).

[76] B. Miller, A. Steinhoff, B. Pano, J. Klein, F. Jahnke, A. Holleitner, and U. Wurstbauer, *Long-Lived Direct and Indirect Interlayer Excitons in van Der Waals Heterostructures*, Nano Lett. **17**, 5229 (2017).

[77] E. Torun, H. P. C. Miranda, A. Molina-Sánchez, and L. Wirtz, *Interlayer and Intralayer Excitons in MoS_2/WS_2 and $MoSe_2/WSe_2$ Heterobilayers*, Phys. Rev. B **97**, 245427 (2018).

[78] C. Jiang, W. Xu, A. Rasmita, Z. Huang, K. Li, Q. Xiong, and W. Gao, *Microsecond Dark-Exciton Valley Polarization Memory in Two-Dimensional Heterostructures*, Nat Commun **9**, 1 (2018).

[79] H. Fang, C. Battaglia, C. Carraro, S. Nemsak, B. Ozdol, J. S. Kang, H. A. Bechtel, S. B. Desai, F. Kronast, A. A. Unal, G. Conti, C. Conlon, G. K. Palsson, M. C. Martin, A. M. Minor, C. S. Fadley, E. Yablonovitch, R. Maboudian, and A. Javey, *Strong Interlayer Coupling in van Der Waals Heterostructures Built from Single-Layer Chalcogenides*, Proceedings of the National Academy of Sciences **111**, 6198 (2014).

[80] X. Hong, J. Kim, S.-F. Shi, Y. Zhang, C. Jin, Y. Sun, S. Tongay, J. Wu, Y. Zhang, and F. Wang, *Ultrafast Charge Transfer in Atomically Thin MoS_2/WS_2 Heterostructures*, Nature Nanotech **9**, 9 (2014).

[81] S. Gao, L. Yang, and C. D. Spataru, *Interlayer Coupling and Gate-Tunable Excitons in Transition Metal Dichalcogenide Heterostructures*, Nano Lett. **17**, 7809 (2017).

[82] Z. Wang, Y.-H. Chiu, K. Honz, K. F. Mak, and J. Shan, *Electrical Tuning of Interlayer Exciton Gases in WSe_2 Bilayers*, Nano Lett. **18**, 137 (2018).

[83] M. Okada, A. Kutana, Y. Kureishi, Y. Kobayashi, Y. Saito, T. Saito, K. Watanabe, T. Taniguchi, S. Gupta, Y. Miyata, B. I. Yakobson, H. Shinohara, and R. Kitaura, *Direct*

and Indirect Interlayer Excitons in a van Der Waals Heterostructure of HBN/WS_2/MoS_2/HBN, ACS Nano **12**, 2498 (2018).

[84] A. T. Hanbicki, H.-J. Chuang, M. R. Rosenberger, C. S. Hellberg, S. V. Sivaram, K. M. McCreary, I. I. Mazin, and B. T. Jonker, *Double Indirect Interlayer Exciton in a $MoSe_2$/WSe_2 van Der Waals Heterostructure*, ACS Nano **12**, 4719 (2018).

[85] C. Choi, J. Huang, H.-C. Cheng, H. Kim, A. K. Vinod, S.-H. Bae, V. O. Özçelik, R. Grassi, J. Chae, S.-W. Huang, X. Duan, K. Kaasbjerg, T. Low, and C. W. Wong, *Enhanced Interlayer Neutral Excitons and Trions in Trilayer van Der Waals Heterostructures*, Npj 2D Mater Appl **2**, 1 (2018).

[86] A. Ciarrocchi, D. Unuchek, A. Avsar, K. Watanabe, T. Taniguchi, and A. Kis, *Polarization Switching and Electrical Control of Interlayer Excitons in Two-Dimensional van Der Waals Heterostructures*, Nature Photon **13**, 2 (2019).

[87] N. Zhang, A. Surrente, M. Baranowski, D. K. Maude, P. Gant, A. Castellanos-Gomez, and P. Plochocka, *Moiré Intralayer Excitons in a $MoSe_2$/MoS_2 Heterostructure*, Nano Lett. **18**, 7651 (2018).

[88] K. Tran, G. Moody, F. Wu, X. Lu, J. Choi, K. Kim, A. Rai, D. A. Sanchez, J. Quan, A. Singh, J. Embley, A. Zepeda, M. Campbell, T. Autry, T. Taniguchi, K. Watanabe, N. Lu, S. K. Banerjee, K. L. Silverman, S. Kim, E. Tutuc, L. Yang, A. H. MacDonald, and X. Li, *Evidence for Moiré Excitons in van Der Waals Heterostructures*, Nature **567**, 7746 (2019).

[89] K. L. Seyler, P. Rivera, H. Yu, N. P. Wilson, E. L. Ray, D. G. Mandrus, J. Yan, W. Yao, and X. Xu, *Signatures of Moiré-Trapped Valley Excitons in $MoSe_2$/WSe_2 Heterobilayers*, Nature **567**, 7746 (2019).

[90] C. Jin, E. C. Regan, D. Wang, M. Iqbal Bakti Utama, C.-S. Yang, J. Cain, Y. Qin, Y. Shen, Z. Zheng, K. Watanabe, T. Taniguchi, S. Tongay, A. Zettl, and F. Wang, *Identification of Spin, Valley and Moiré Quasi-Angular Momentum of Interlayer Excitons*, Nat. Phys. **15**, 11 (2019).

[91] E. M. Alexeev, D. A. Ruiz-Tijerina, M. Danovich, M. J. Hamer, D. J. Terry, P. K. Nayak, S. Ahn, S. Pak, J. Lee, J. I. Sohn, M. R. Molas, M. Koperski, K. Watanabe, T. Taniguchi, K. S. Novoselov, R. V. Gorbachev, H. S. Shin, V. I. Fal'ko, and A. I. Tartakovskii, *Resonantly Hybridized Excitons in Moiré Superlattices in van Der Waals Heterostructures*, Nature **567**, 7746 (2019).

[92] C. Jin, E. C. Regan, A. Yan, M. Iqbal Bakti Utama, D. Wang, S. Zhao, Y. Qin, S. Yang, Z. Zheng, S. Shi, K. Watanabe, T. Taniguchi, S. Tongay, A. Zettl, and F. Wang, *Observation of Moiré Excitons in WSe_2/WS_2 Heterostructure Superlattices*, Nature **567**, 7746 (2019).

[93] F. Wu, T. Lovorn, and A. H. MacDonald, *Topological Exciton Bands in Moir\'e Heterojunctions*, Phys. Rev. Lett. **118**, 147401 (2017).

[94] H. Yu, G.-B. Liu, and W. Yao, *Brightened Spin-Triplet Interlayer Excitons and Optical Selection Rules in van Der Waals Heterobilayers*, 2D Mater. **5**, 035021 (2018).

[95] I. B. Spielman, J. P. Eisenstein, L. N. Pfeiffer, and K. W. West, *Resonantly Enhanced Tunneling in a Double Layer Quantum Hall Ferromagnet*, Phys. Rev. Lett. **84**, 5808 (2000).

[96] M. Kellogg, J. P. Eisenstein, L. N. Pfeiffer, and K. W. West, *Vanishing Hall Resistance at High Magnetic Field in a Double-Layer Two-Dimensional Electron System*, Phys. Rev. Lett. **93**, 036801 (2004).

[97] E. Tutuc, M. Shayegan, and D. A. Huse, *Counterflow Measurements in Strongly Correlated GaAs Hole Bilayers: Evidence for Electron-Hole Pairing*, Phys. Rev. Lett. **93**, 036802 (2004).

[98] J. P. Eisenstein and A. H. MacDonald, *Bose–Einstein Condensation of Excitons in Bilayer Electron Systems*, Nature **432**, 7018 (2004).

[99] L. Tiemann, J. G. S. Lok, W. Dietsche, K. von Klitzing, K. Muraki, D. Schuh, and W. Wegscheider, *Exciton Condensate at a Total Filling Factor of One in Corbino Two-Dimensional Electron Bilayers*, Phys. Rev. B **77**, 033306 (2008).

[100] D. Nandi, A. D. K. Finck, J. P. Eisenstein, L. N. Pfeiffer, and K. W. West, *Exciton Condensation and Perfect Coulomb Drag*, Nature **488**, 7412 (2012).

[101] X. Liu, K. Watanabe, T. Taniguchi, B. I. Halperin, and P. Kim, *Quantum Hall Drag of Exciton Condensate in Graphene*, Nature Phys **13**, 8 (2017).

[102] J. I. A. Li, T. Taniguchi, K. Watanabe, J. Hone, and C. R. Dean, *Excitonic Superfluid Phase in Double Bilayer Graphene*, Nature Phys **13**, 8 (2017).

[103] G.-B. Liu, W.-Y. Shan, Y. Yao, W. Yao, and D. Xiao, *Three-Band Tight-Binding Model for Monolayers of Group-VIB Transition Metal Dichalcogenides*, Phys. Rev. B **88**, 085433 (2013).

[104] G. Wang, C. Robert, A. Suslu, B. Chen, S. Yang, S. Alamdari, I. C. Gerber, T. Amand, X. Marie, S. Tongay, and B. Urbaszek, *Spin-Orbit Engineering in Transition Metal Dichalcogenide Alloy Monolayers*, Nat Commun **6**, 1 (2015).

[105] X.-X. Zhang, Y. You, S. Y. F. Zhao, and T. F. Heinz, *Experimental Evidence for Dark Excitons in Monolayer WSe_2*, Phys. Rev. Lett. **115**, 257403 (2015).

[106] Y. Zhou, G. Scuri, D. S. Wild, A. A. High, A. Dibos, L. A. Jauregui, C. Shu, K. De Greve, K. Pistunova, A. Y. Joe, T. Taniguchi, K. Watanabe, P. Kim, M. D. Lukin, and H. Park, *Probing Dark Excitons in Atomically Thin Semiconductors via Near-Field Coupling to Surface Plasmon Polaritons*, Nature Nanotech **12**, 9 (2017).

[107] X.-X. Zhang, T. Cao, Z. Lu, Y.-C. Lin, F. Zhang, Y. Wang, Z. Li, J. C. Hone, J. A. Robinson, D. Smirnov, S. G. Louie, and T. F. Heinz, *Magnetic Brightening and Control of Dark Excitons in Monolayer WSe_2*, Nature Nanotech **12**, 9 (2017).

[108] T. Huber, A. Zrenner, W. Wegscheider, and M. Bichler, *Electrostatic Exciton Traps*, Physica Status Solidi **166**, R5 (1998).

[109] A. V. Gorbunov and V. B. Timofeev, *Interwell Excitons in a Lateral Potential Well in an Inhomogeneous Electric Field*, Jetp Lett. **80**, 185 (2004).

[110] A. A. High, J. R. Leonard, M. Remeika, L. V. Butov, M. Hanson, and A. C. Gossard, *Condensation of Excitons in a Trap*, Nano Lett. **12**, 2605 (2012).

[111] G. J. Schinner, J. Repp, E. Schubert, A. K. Rai, D. Reuter, A. D. Wieck, A. O. Govorov, A. W. Holleitner, and J. P. Kotthaus, *Confinement and Interaction of Single Indirect Excitons in a Voltage-Controlled Trap Formed Inside Double InGaAs Quantum Wells*, Phys. Rev. Lett. **110**, 127403 (2013).

[112] Y. Shilo, K. Cohen, B. Laikhtman, K. West, L. Pfeiffer, and R. Rapaport, *Particle Correlations and Evidence for Dark State Condensation in a Cold Dipolar Exciton Fluid*, Nat Commun **4**, 1 (2013).

[113] Y. Mazuz-Harpaz, K. Cohen, B. Laikhtman, R. Rapaport, K. West, and L. N. Pfeiffer, *Radiative Lifetimes of Dipolar Excitons in Double Quantum Wells*, Phys. Rev. B **95**, 155302 (2017).

[114] Z. Y. Zhu, Y. C. Cheng, and U. Schwingenschlögl, *Giant Spin-Orbit-Induced Spin Splitting in Two-Dimensional Transition-Metal Dichalcogenide Semiconductors*, Phys. Rev. B **84**, 153402 (2011).

[115] O. Witham, R. J. Hunt, and N. D. Drummond, *Stability of Trions in Coupled Quantum Wells Modeled by Two-Dimensional Bilayers*, Phys. Rev. B **97**, 075424 (2018).

[116] I. V. Bondarev and M. R. Vladimirova, *Complexes of Dipolar Excitons in Layered Quasi-Two-Dimensional Nanostructures*, Phys. Rev. B **97**, 165419 (2018).

[117] K. F. Mak, K. He, C. Lee, G. H. Lee, J. Hone, T. F. Heinz, and J. Shan, *Tightly Bound Trions in Monolayer MoS_2*, Nature Mater **12**, 3 (2013).

[118] J. S. Ross, S. Wu, H. Yu, N. J. Ghimire, A. M. Jones, G. Aivazian, J. Yan, D. G. Mandrus, D. Xiao, W. Yao, and X. Xu, *Electrical Control of Neutral and Charged Excitons in a Monolayer Semiconductor*, Nat Commun **4**, 1 (2013).

[119] T. C. Berkelbach, M. S. Hybertsen, and D. R. Reichman, *Theory of Neutral and Charged Excitons in Monolayer Transition Metal Dichalcogenides*, Phys. Rev. B **88**, 045318 (2013).

[120] E. Courtade, M. Semina, M. Manca, M. M. Glazov, C. Robert, F. Cadiz, G. Wang, T. Taniguchi, K. Watanabe, M. Pierre, W. Escoffier, E. L. Ivchenko, P. Renucci, X. Marie, T. Amand, and B. Urbaszek, *Charged Excitons in Monolayer WSe_2: Experiment and Theory*, Phys. Rev. B **96**, 085302 (2017).

[121] D. Yoshioka and A. H. MacDonald, *Double Quantum Well Electron-Hole Systems in Strong Magnetic Fields*, Journal of the Physical Society of Japan **59**, 4211 (1990).

[122] X. Zhu, P. B. Littlewood, M. S. Hybertsen, and T. M. Rice, *Exciton Condensate in Semiconductor Quantum Well Structures*, Phys. Rev. Lett. **74**, 1633 (1995).

[123] Yu. E. Lozovik and O. L. Berman, *Phase Transitions in a System of Two Coupled Quantum Wells*, Jetp Lett. **64**, 573 (1996).

[124] T. Godde, D. Schmidt, J. Schmutzler, M. Aßmann, J. Debus, F. Withers, E. M. Alexeev, O. Del Pozo-Zamudio, O. V. Skrypka, and K. S. Novoselov, *Exciton and Trion Dynamics in Atomically Thin $MoSe_2$ and WSe_2: Effect of Localization*, Physical Review B **94**, 165301 (2016).

[125] C. Robert, D. Lagarde, F. Cadiz, G. Wang, B. Lassagne, T. Amand, A. Balocchi, P. Renucci, S. Tongay, B. Urbaszek, and X. Marie, *Exciton Radiative Lifetime in Transition Metal Dichalcogenide Monolayers*, Phys. Rev. B **93**, 205423 (2016).

[126] M. Palummo, M. Bernardi, and J. C. Grossman, *Exciton Radiative Lifetimes in Two-Dimensional Transition Metal Dichalcogenides*, Nano Lett. **15**, 2794 (2015).

[127] Z. Vörös, R. Balili, D. W. Snoke, L. Pfeiffer, and K. West, *Long-Distance Diffusion of Excitons in Double Quantum Well Structures*, Phys. Rev. Lett. **94**, 226401 (2005).

[128] S. Lazić, P. V. Santos, and R. Hey, *Exciton Transport by Moving Strain Dots in GaAs Quantum Wells*, Physica E: Low-Dimensional Systems and Nanostructures **42**, 2640 (2010).

[129] A. V. Gorbunov, V. B. Timofeev, and D. A. Demin, *Electro-Optical Trap for Dipolar Excitons in a GaAs/AlAs Schottky Diode with a Single Quantum Well*, Jetp Lett. **94**, 800 (2012).

[130] M. Alloing, A. Lemaître, E. Galopin, and F. Dubin, *Nonlinear Dynamics and Inner-Ring Photoluminescence Pattern of Indirect Excitons*, Phys. Rev. B **85**, 245106 (2012).

[131] S. Zimmermann, G. Schedelbeck, A. O. Govorov, A. Wixforth, J. P. Kotthaus, M. Bichler, W. Wegscheider, and G. Abstreiter, *Spatially Resolved Exciton Trapping in a Voltage-Controlled Lateral Superlattice*, Appl. Phys. Lett. **73**, 154 (1998).

[132] M. Remeika, M. M. Fogler, L. V. Butov, M. Hanson, and A. C. Gossard, *Two-Dimensional Electrostatic Lattices for Indirect Excitons*, Appl. Phys. Lett. **100**, 061103 (2012).

[133] X. P. Vögele, D. Schuh, W. Wegscheider, J. P. Kotthaus, and A. W. Holleitner, *Density Enhanced Diffusion of Dipolar Excitons within a One-Dimensional Channel*, Phys. Rev. Lett. **103**, 126402 (2009).

[134] K. Cohen, R. Rapaport, and P. V. Santos, *Remote Dipolar Interactions for Objective Density Calibration and Flow Control of Excitonic Fluids*, Phys. Rev. Lett. **106**, 126402 (2011).

[135] C. J. Dorow, J. R. Leonard, M. M. Fogler, L. V. Butov, K. W. West, and L. N. Pfeiffer, *Split-Gate Device for Indirect Excitons*, Appl. Phys. Lett. **112**, 183501 (2018).

[136] R. Bistritzer and A. H. MacDonald, *Moir\'e Butterflies in Twisted Bilayer Graphene*, Phys. Rev. B **84**, 035440 (2011).

[137] P. Rivera, H. Yu, K. L. Seyler, N. P. Wilson, W. Yao, and X. Xu, *Interlayer Valley Excitons in Heterobilayers of Transition Metal Dichalcogenides*, Nature Nanotech **13**, 11 (2018).

[138] E. V. Calman, L. H. Fowler-Gerace, D. J. Choksy, L. V. Butov, D. E. Nikonov, I. A. Young, S. Hu, A. Mishchenko, and A. K. Geim, *Indirect Excitons and Trions in MoSe2/WSe2 van Der Waals Heterostructures*, Nano Lett. **20**, 1869 (2020).

[139] N. Kumar, Q. Cui, F. Ceballos, D. He, Y. Wang, and H. Zhao, *Exciton Diffusion in Monolayer and Bulk $MoSe_2$*, Nanoscale **6**, 4915 (2014).

[140] M. Kulig, J. Zipfel, P. Nagler, S. Blanter, C. Schüller, T. Korn, N. Paradiso, M. M. Glazov, and A. Chernikov, *Exciton Diffusion and Halo Effects in Monolayer Semiconductors*, Phys. Rev. Lett. **120**, 207401 (2018).

[141] F. Cadiz, C. Robert, E. Courtade, M. Manca, L. Martinelli, T. Taniguchi, K. Watanabe, T. Amand, A. C. H. Rowe, D. Paget, B. Urbaszek, and X. Marie, *Exciton Diffusion in WSe_2 Monolayers Embedded in a van Der Waals Heterostructure*, Appl. Phys. Lett. **112**, 152106 (2018).

[142] D. F. Cordovilla Leon, Z. Li, S. W. Jang, C.-H. Cheng, and P. B. Deotare, *Exciton Transport in Strained Monolayer WSe_2*, Appl. Phys. Lett. **113**, 252101 (2018).

[143] D. F. Cordovilla Leon, Z. Li, S. W. Jang, and P. B. Deotare, *Hot Exciton Transport in WSe_2 Monolayers*, Phys. Rev. B **100**, 241401 (2019).

[144] S. Hao, M. Z. Bellus, D. He, Y. Wang, and H. Zhao, *Controlling Exciton Transport in Monolayer $MoSe_2$ by Dielectric Screening*, Nanoscale Horiz. **5**, 139 (2019).

[145] Y. Tang, L. Li, T. Li, Y. Xu, S. Liu, K. Barmak, K. Watanabe, T. Taniguchi, A. H. MacDonald, J. Shan, and K. F. Mak, *Simulation of Hubbard Model Physics in WSe_2/WS_2 Moiré Superlattices*, Nature **579**, 7799 (2020).

[146] D. M. Kennes, M. Claassen, L. Xian, A. Georges, A. J. Millis, J. Hone, C. R. Dean, D. N. Basov, A. N. Pasupathy, and A. Rubio, *Moiré Heterostructures as a Condensed-Matter Quantum Simulator*, Nat. Phys. **17**, 2 (2021).

[147] J. S. Alden, A. W. Tsen, P. Y. Huang, R. Hovden, L. Brown, J. Park, D. A. Muller, and P. L. McEuen, *Strain Solitons and Topological Defects in Bilayer Graphene*, Proceedings of the National Academy of Sciences **110**, 11256 (2013).

[148] C. R. Woods, L. Britnell, A. Eckmann, R. S. Ma, J. C. Lu, H. M. Guo, X. Lin, G. L. Yu, Y. Cao, R. V. Gorbachev, A. V. Kretinin, J. Park, L. A. Ponomarenko, M. I. Katsnelson, Y. N. Gornostyrev, K. Watanabe, T. Taniguchi, C. Casiraghi, H.-J. Gao, A. K. Geim, and K. S. Novoselov, *Commensurate–Incommensurate Transition in Graphene on Hexagonal Boron Nitride*, Nature Phys **10**, 6 (2014).

[149] A. Weston, Y. Zou, V. Enaldiev, A. Summerfield, N. Clark, V. Zólyomi, A. Graham, C. Yelgel, S. Magorrian, M. Zhou, J. Zultak, D. Hopkinson, A. Barinov, T. H. Bointon, A. Kretinin, N. R. Wilson, P. H. Beton, V. I. Fal'ko, S. J. Haigh, and R. Gorbachev, *Atomic Reconstruction in Twisted Bilayers of Transition Metal Dichalcogenides*, Nat. Nanotechnol. **15**, 7 (2020).

[150] H. Yoo, R. Engelke, S. Carr, S. Fang, K. Zhang, P. Cazeaux, S. H. Sung, R. Hovden, A. W. Tsen, T. Taniguchi, K. Watanabe, G.-C. Yi, M. Kim, M. Luskin, E. B. Tadmor, E. Kaxiras, and P. Kim, *Atomic and Electronic Reconstruction at the van Der Waals Interface in Twisted Bilayer Graphene*, Nat. Mater. **18**, 5 (2019).

[151] T. Korn, S. Heydrich, M. Hirmer, J. Schmutzler, and C. Schüller, *Low-Temperature Photocarrier Dynamics in Monolayer MoS_2*, Appl. Phys. Lett. **99**, 102109 (2011).

[152] A. Zrenner, L. V. Butov, M. Hagn, G. Abstreiter, G. Böhm, and G. Weimann, *Quantum Dots Formed by Interface Fluctuations in AlAs/GaAs Coupled Quantum Well Structures*, Phys. Rev. Lett. **72**, 3382 (1994).

[153] A. V. Larionov, V. B. Timofeev, J. Hvam, and K. Soerensen, *Interwell Excitons in GaAs/AlGaAs Double Quantum Wells and Their Collective Properties*, J. Exp. Theor. Phys. **90**, 1093 (2000).

[154] J. R. Leonard, Y. Y. Kuznetsova, S. Yang, L. V. Butov, T. Ostatnický, A. Kavokin, and A. C. Gossard, *Spin Transport of Excitons*, Nano Lett. **9**, 4204 (2009).

[155] R. Finkelstein, K. Cohen, B. Jouault, K. West, L. N. Pfeiffer, M. Vladimirova, and R. Rapaport, *Transition from Spin-Orbit to Hyperfine Interaction Dominated Spin Relaxation in a Cold Fluid of Dipolar Excitons*, Phys. Rev. B **96**, 085404 (2017).

[156] F. Fedichkin, P. Andreakou, B. Jouault, M. Vladimirova, T. Guillet, C. Brimont, P. Valvin, T. Bretagnon, A. Dussaigne, N. Grandjean, and P. Lefebvre, *Transport of Dipolar Excitons in (Al,Ga)N/GaN Quantum Wells*, Phys. Rev. B **91**, 205424 (2015).

[157] Y. Y. Kuznetsova, F. Fedichkin, P. Andreakou, E. V. Calman, L. V. Butov, P. Lefebvre, T. Bretagnon, T. Guillet, M. Vladimirova, C. Morhain, and J.-M. Chauveau, *Transport of Indirect Excitons in ZnO Quantum Wells*, Opt. Lett., OL **40**, 3667 (2015).

[158] M. Goryca, J. Li, A. V. Stier, T. Taniguchi, K. Watanabe, E. Courtade, S. Shree, C. Robert, B. Urbaszek, X. Marie, and S. A. Crooker, *Revealing Exciton Masses and Dielectric Properties of Monolayer Semiconductors with High Magnetic Fields*, Nat Commun **10**, 1 (2019).

[159] K. Datta, Z. Lyu, Z. Li, T. Taniguchi, K. Watanabe, and P. B. Deotare, *Spatiotemporally Controlled Room-Temperature Exciton Transport under Dynamic Strain*, Nat. Photon. **16**, 3 (2022).

[160] N. P. Wilson, W. Yao, J. Shan, and X. Xu, *Excitons and Emergent Quantum Phenomena in Stacked 2D Semiconductors*, Nature **599**, 7885 (2021).

[161] L. H. Fowler-Gerace, D. J. Choksy, and L. V. Butov, *Voltage-Controlled Long-Range Propagation of Indirect Excitons in a van Der Waals Heterostructure*, Phys. Rev. B **104**, 165302 (2021).

[162] D. J. Choksy, C. Xu, M. M. Fogler, L. V. Butov, J. Norman, and A. C. Gossard, *Attractive and Repulsive Dipolar Interaction in Bilayers of Indirect Excitons*, Phys. Rev. B **103**, 045126 (2021).

[163] A. Kormányos, G. Burkard, M. Gmitra, J. Fabian, V. Zólyomi, N. D. Drummond, and V. Fal'ko, ***K·p*** *Theory for Two-Dimensional Transition Metal Dichalcogenide Semiconductors*, 2D Mater. **2**, 022001 (2015).

[164] P. V. Nguyen, N. C. Teutsch, N. P. Wilson, J. Kahn, X. Xia, A. J. Graham, V. Kandyba, A. Giampietri, A. Barinov, G. C. Constantinescu, N. Yeung, N. D. M. Hine, X. Xu, D. H.

Cobden, and N. R. Wilson, *Visualizing Electrostatic Gating Effects in Two-Dimensional Heterostructures*, Nature **572**, 7768 (2019).

[165] J. Wang, J. Ardelean, Y. Bai, A. Steinhoff, M. Florian, F. Jahnke, X. Xu, M. Kira, J. Hone, and X.-Y. Zhu, *Optical Generation of High Carrier Densities in 2D Semiconductor Heterobilayers*, Science Advances **5**, eaax0145 (2019).

[166] D. E. Nikonov and A. Imamoglu, *Bose Condensation in Two Dimensions with Disorder: Gross-Pitaevskii Approach*, arXiv:quant-ph/9806003.

[167] C. J. Dorow, M. W. Hasling, E. V. Calman, L. V. Butov, J. Wilkes, K. L. Campman, and A. C. Gossard, *Spatially Resolved and Time-Resolved Imaging of Transport of Indirect Excitons in High Magnetic Fields*, Phys. Rev. B **95**, 235308 (2017).

[168] D. S. Fisher and P. C. Hohenberg, *Dilute Bose Gas in Two Dimensions*, Phys. Rev. B **37**, 4936 (1988).

[169] A. L. Ivanov, *Quantum Diffusion of Dipole-Oriented Indirect Excitons in Coupled Quantum Wells*, EPL **59**, 586 (2002).

[170] A. T. Hammack, L. V. Butov, J. Wilkes, L. Mouchliadis, E. A. Muljarov, A. L. Ivanov, and A. C. Gossard, *Kinetics of the Inner Ring in the Exciton Emission Pattern in Coupled GaAs Quantum Wells*, Phys. Rev. B **80**, 155331 (2009).